Title

Structure and Dynamics of the Aβ21–30 Peptide from the Interplay of NMR Experiments and Molecular Simulations

Journal

Journal of the American Chemical Society, 130(19)

ISSN

0002-7863

Authors

Fawzi, Nicolas L
Phillips, Aaron H
Ruscio, Jory Z
et al.

Publication Date

2008-05-01

DOI

10.1021/ja710366c

Peer reviewed

STRUCTURE AND DYNAMICS OF THE $A\beta_{21-30}$ PEPTIDE FROM THE INTERPLAY OF NMR EXPERIMENTS AND MOLECULAR SIMULATIONS

Nicolas Lux Fawzi[1], Aaron H. Phillips[2], Jory Z. Ruscio[3], Michaeleen Doucleff[2], David E. Wemmer[2,4], Teresa Head-Gordon[1,3,4,*]

[1]UCSF/UCB Joint Graduate Group in Bioengineering, Berkeley, CA 94720
[2]Department of Chemistry, University of California, Berkeley, CA 94720
[3]Department of Bioengineering, University of California, Berkeley, CA 94720
[4]Physical Biosciences Division, Lawrence Berkeley National Laboratory
Berkeley CA 94720

We combine molecular dynamics simulations and new high field NMR experiments to describe the solution structure of the $A\beta_{21-30}$ peptide fragment that may be relevant for understanding structural mechanisms related to Alzheimer's Disease. Using two different empirical force field combinations we provide predictions of the three bond scalar coupling constants ($^3J_{HNH\alpha}$), chemical shift values, ^{13}C relaxation parameters, and ROESY cross peaks that can then be compared directly to the same observables measured in the corresponding NMR experiment of $A\beta_{21-30}$. We find robust prediction of the ^{13}C relaxation parameters and medium-range ROESY cross peaks using new generation TIP4P-Ew water and Amber ff99SB protein force fields, in which the NMR validates that the simulation yields both a structurally and dynamically correct ensemble over the entire $A\beta_{21-30}$ peptide. Analysis of the simulated ensemble shows that all medium-range ROE restraints are not satisfied simultaneously, and demonstrates the structural diversity of the $A\beta_{21-30}$ conformations more completely than when determined from the experimental medium-range ROE restraints alone. We find that the structural ensemble of the $A\beta_{21-30}$ peptide involves a majority population (~60%) of unstructured conformers, lacking any secondary structure or persistent hydrogen-bonding networks. However the remaining minority population contains a substantial percentage of conformers with a β-turn centered at Val24 and Gly25, as well as evidence of the Asp23 to Lys28 salt bridge important to the fibril structure. This study sets the stage for robust theoretical work on $A\beta_{1-40}$ and $A\beta_{1-42}$, for which collection of detailed NMR data on the monomer will be more challenging due to aggregation and fibril formation on experimental timescales at physiological conditions. In addition, we believe that the interplay of modern molecular simulation and high quality NMR experiments have reached a fruitful stage for characterizing structural ensembles of disordered peptides and proteins in general.

***Corresponding author**

INTRODUCTION

The amyloid β (Aβ) peptide, comprised of a family of 39 to 42 residue long fragments cleaved by proteolysis of the APP protein, is the major species in amyloid fibril plaque found in the brains of patients with Alzheimer's disease (AD)[1, 2]. However, recent evidence suggests that it may be the pre-fibrillar monomer and oligomeric states of the Aβ peptides, as opposed to the actual fibril plaque[3], that give rise to the cytotoxicity of the Alzheimer's disease state[4-9]. Therefore knowledge of the structural ensembles of the Aβ peptide on the aggregation pathways from monomer to fibril is critical for understanding aggregation outcomes *in vitro*, with the hope of potentially changing the course of the disease *in vivo*.

While significant progress has been made in the characterization of highly ordered amyloid fibril structures of Aβ peptides under physiological conditions[3, 10-14], the aqueous monomeric form is difficult to study by standard structural biology techniques due to its propensity to sequester into these ordered fibril assemblies. While recent studies by NMR spectroscopy have found some regular structure in the $A\beta_{1-40}$ and $A\beta_{1-42}$ monomer peptides in high concentrations of non-aqueous solvents (hexafluoroisopropanol, trifluroethanol, SDS micelles)[15-18], these may or may not be relevant to the correct physiological conditions. Other studies have calculated averaged quantities such as scalar coupling constants[19] and spin relaxation constants[20, 21] for aqueous solution ensembles of the peptide, but these data measure only local rather than tertiary structure and hence provide an incomplete description of the structural ensemble.

In an attempt to probe for any significant structure in the monomeric state by an alternative technique, Lazo *et al*. subjected the $A\beta_{1-40}$ and $A\beta_{1-42}$ peptides to digestion by multiple proteases[22]. Despite containing a large number of potential proteolytic sites throughout the sequence, it was determined that the peptide fragment spanning residues 21 to 30 (AEDVGSNKGA) was a significant product for each enzyme, indicating relative resistance to cleavage. Furthermore, little digestion was seen when the synthetic $A\beta_{21-30}$ fragment itself was subjected to the same protease conditions. These results were interpreted to mean that some structure in the 21 to 30 region protects $A\beta_{1-40}$ and $A\beta_{1-42}$ from protease degradation, and that this structure is retained in the $A\beta_{21-30}$ fragment[22].

One of the primary benefits of studying this small zwitterionic peptide fragment is that it is readily soluble in its monomeric form at concentrations in which the longer and more hydrophobic $A\beta_{1-40}$ and $A\beta_{1-42}$ sequences aggregate. In addition, many of the amino acids thought to be important for understanding the AD state are part of the $A\beta_{21-30}$ fragment. The $A\beta_{21-30}$ sequence consists mainly of a

hydrophilic region that, in the context of the fibril structure of the full-length $A\beta_{1-40}$, comprises a turn connecting the two flanking hydrophobic β-strand regions that is necessary for generating the observed cross-β structure down the fibril axis[11]. Additionally, the buried salt bridge between Asp23 and Lys28 in the fibrillar form, determined by solid state NMR[11, 13, 23], is also encompassed by this peptide. It has been shown that mutating either residue dramatically affects fibril formation[23, 24]. It is also noteworthy that many of the familial associated disease (FAD) mutants of the APP protein are located between residues 21 to 23, each of which leads to dramatically different *in vitro* fibril formation properties[25] and *in vivo* clinical outcomes[24, 26-34].

A number of experimental and computational studies have attempted to determine what stable structure in the $A\beta_{21-30}$ monomer accounts for its protease resistance. Teplow and co-workers studied the wild-type[22] as well as five FAD mutants[35] of the $A\beta_{21-30}$ peptide using rotating frame nuclear Overhauser effect spectroscopy (ROESY) NMR experiments. They proposed that WT $A\beta_{21-30}$ folds into a single conformer corresponding to a unique bend structure, identified through long range (i,i+8) crosspeaks for Glu22 H_α to Ala30 HN, and (i,i+6) sidechain-sidechain crosspeaks for Glu22 to Lys28 in the ROESY spectrum of WT $A\beta_{21-30}$; these crosspeaks were found to be absent in the FAD mutants[35]. Replica exchange molecular dynamics simulations by Baumketner et al. using the OPLS and TIP3P all-atom models for peptide and water[36], found that 40% of the peptide ensemble is folded into two distinct bend structures stabilized primarily by Asp23 sidechain interactions with the Ser26 sidechain and backbone. Borreguero and coworkers studied the peptide by a coarse-grained model in which they find collapsed structures stabilized by hydrophobic interactions between Val24 and Lys28, as well as electrostatic interactions between Asp23 to Lys28[37]. They also simulated five ~100 ns molecular dynamics trajectories using CHARMM-27 and TIP3P for the peptide and water model, without using any accelerated sampling technique, each with a different combination of density, starting structure and salt concentration[38]. Though the authors acknowledge that their simulations are far too short to converge to the equilibrium ensemble, they report contacts between hydrophobic regions of Val24 and Lys28 that are more stable on the nanosecond timescale than charged interactions between Lys28 and Glu22 or Asp23. Finally Mousseau, Derreumaux and coworkers used an activation-relaxation sampling technique combined with the OPEP coarse-grained model of $A\beta_{21-30}$ and found several clusters of structures, all sharing a turn formed by stabilizing interactions between Val24 and Lys28 of many different sidechain contact combinations[39]. In summary, simulations found little

evidence of the long-range interactions observed in the NMR experiment but provided little consensus on the solution structure of the $A\beta_{21-30}$ peptide.

In this study we present new NMR experimental measurements on the aqueous $A\beta_{21-30}$ peptide fragment, including three bond scalar coupling constants ($^3J_{HNH\alpha}$), chemical shift values, ^{13}C relaxation parameters, and ROESY spectra measured at 800 and 900MHz. We determine that while there are a handful of medium-range ROEs, no long range (i,i+8) or (i,i+6) crosspeaks are present, nor are there patterns of α-helical or β-sheet contacts, indicating that the structural ensemble for the $A\beta_{21-30}$ fragment is highly diverse. We quantify this structural diversity of $A\beta_{21-30}$ by molecular dynamics simulations using two different water models, which are validated by calculating the same NMR observables from demonstrably converged equilibrium structural and dynamical ensembles. We find that the Amber ff99SB[40] protein and TIP4P-Ew[41] water models provide robust prediction of the measured ^{13}C relaxation parameters and ROESY cross peaks in particular, indicating that they yield both a structurally and dynamically correct ensemble over the entire $A\beta_{21-30}$ peptide.

The interplay of the high quality NMR experiments and the validated theoretical model allow us to analyze the simulated structural ensemble and show that the medium-range ROE interactions are not satisfied simultaneously. In fact they arise from separate structural populations of local turn structure in regions 23 to 27 and 27 to 30 that together comprise only ~40% of the total equilibrium ensemble, and thus provide a qualitatively different result from the single structural model reported by Lazo and coworkers[22, 35]. The very good quality of results of this validation study on $A\beta_{21-30}$ paves the way for simulating the structural ensemble of the $A\beta_{1-40}$ and $A\beta_{1-42}$ systems, since solution NMR experiments on these peptides are inherently more difficult due to peptide aggregation. Furthermore we believe that this study shows that the interplay of modern molecular simulation and high quality NMR experiments have reached a fruitful stage for characterizing structural ensembles of disordered peptides and proteins in general.

METHODS

NMR Experiments

The $A\beta_{21-30}$ peptide (AEDVGSNKGA) was synthesized (Anaspec, San Jose CA) and purified to 98% purity by reverse-phase HPLC. NMR samples contained 10 mM $A\beta_{21-30}$ and 25 mM ammonium d_4-acetate in 90% H_2O, 10% ^2H_2O or 100% ^2H_2O. The solution pH was adjusted to 6.0 with 20 μl 1M NaOH. NMR data were collected at 283 K on a Bruker Avance 500 MHz and Bruker Avance II 800 or

900 MHz spectrometers. All data were processed with NMRPipe[42] and analyzed with NMRView[43] and CARA[44]. All spectra were recorded at 10°C to facilitate comparison with previous NMR studies on this peptide.

Chemical shift assignments were obtained with a 2D ^{1}H-^{1}H TOCSY. Distance restraints were obtained from two 2D ^{1}H-^{1}H ROESY experiments in both 90% H_2O, 10% $^{2}H_2O$ and 100% $^{2}H_2O$ with a composite pulse spinlock[45] applied during the 300 ms mixing time. Additional H_2O ROESY spectra were also collected with 200 and 400 ms mixing times but were not used in generating distance restraints. A total of 4096 and 1400 points (States-TPPI) were collected in t_2 and t_1, respectively. Spectral widths in both dimensions were 7184 and 8503 Hz on the 800 and 900 MHz spectrometers, respectively.

To build a single structural model fitting all of the data simultaneously using a standard NMR structure determination approach, ROESY crosspeaks were classified as strong, medium, weak, and very weak based on peak intensity and converted to 2.9, 3.3, 5.0, and 6.0 Å upper distance restraints, respectively. The set of 155 manually assigned distant restraints was used to calculate 1000 structures with the program CYANA[46]. The 50 lowest energy structures of the minimized ensemble were analyzed with the program Pymol[47]. Structural statistics and hydrogen bonds present in the structure ensemble, detected with the Amber suite[48] program *ptraj* are presented in the Results.

Spin-lattice (T_1) and spin-spin (T_2) relaxation times for natural abundance ^{13}C at the C_α position were measured for all non-glycine amino acids using the same 100% $^{2}H_2O$ sample described above. T_1 was measured at 500 MHz by inverse-detected inversion recovery with delay times 5, 25, 50, 150, 400, 600, 1000, 2000, and 2500 ms[49]. T_2 was measured at 600MHz by an inverse-detected CPMG experiment with delay times 0, 20.48, 40.96, 61.44, 82.92, 122.88, 143.36, 163.84, 204.8 ms[49]. Relaxation parameters were fit from the data as described previously[49].

Three bond scalar coupling constants $^{3}J_{H^N H^\alpha}$ were measured from the multiplet structure in a 2D double-quantum filtered COSY measured at 500 MHz with a spectral width of 6127 Hz in both dimensions. To ensure that the experimental lineshape was not adversely affected by limited digital resolution 4096 points were collected in both t_1 and t_2. Quadrature detection in t_1 was obtained according to the States-TPPI method and the digital resolution was matched to t_2 with linear prediction.

Simulation Protocol

We represent the zwitterionic $A\beta_{21-30}$ peptide using the Amber ff99SB fixed charge empirical force field[40]. Amber ff99SB is a recent reparameterization of the backbone dihedral angles of proteins

by Simmerling and coworkers to correct previous problems with secondary structure propensities of the original ff99 parameters. Amber ff99SB quantitatively captures the distribution of backbone ϕ/ψ angles compared with quantum mechanical calculations and validation on model peptide and protein systems. We have chosen to run two separate sets of simulations where we solvate the peptide with TIP3P[50] and TIP4P-Ew[41] water models, respectively. TIP3P is an older water model that is popularly used in aqueous protein simulations, while TIP4P-Ew is a newer re-parameterized version of the standard TIP4P water model for use with Ewald summation techniques. We chose TIP4P-Ew as the alternate water model since it reproduces many salient thermodynamic and dynamic features of bulk water properties when compared with experiment[41], and its excellent performance for temperature trends of these properties is especially relevant for this experimental study which is conducted at 10°C.

In this work we use the AMBER9 molecular dynamics simulation package[48] to generate the structural and dynamical ensembles of $A\beta_{21\text{-}30}$ peptide fragment in water. The system is prepared by solvating the $A\beta_{21\text{-}30}$ structure with 1578 TIP3P or 1579 TIP4P-Ew water molecules, respectively. A single sodium (Na^+) ion is included in the system to balance the peptide net charge. Each system is briefly equilibrated using Andersen thermostats[51] to bring the system up to 300K temperature, then equilibrated for 125ps at constant pressure with Berendsen (weak) coupling at 1 bar (default parameters) and 300K temperature to determine the density. The average density of the last 100ps of the constant pressure simulation is then calculated and a snapshot containing position and velocity information with that density (within $0.001 g/cm^3$) is selected as the starting structure for further equilibration in the NVT ensemble. In all simulations the equations of motion are integrated with 1fs timesteps, the long-range electrostatic interactions are calculated using Particle Mesh Ewald method (PME)[52], and a cutoff of 9.0 Å is used for real space electrostatics and LJ interactions.

We use replica exchange[53, 54] through the *sander* module of Amber9 to improve convergence at the lower temperatures, using 64 temperature replicas exponentially spaced between 270 K and 507 K with exchange attempts every 1 ps. We ran two independent replica exchange simulations for a time between 45ns and 50ns per replica, of which the first 20ns of each replica is treated as equilibration. The second replica exchange simulation was started from configurations acquired after 20ns equilibration in the first replica exchange simulation, but using a new set of randomized velocities. We measure convergence to equilibrium of the two independent simulations by whether they both reach the same linear average of the pair distances over their structural ensembles. We find that the equilibrium populations of the two independent runs differ by no more than 7% in this quantity. We

comment later on the challenge of converging these averages and their effect on the predictions of NMR observables in the Results.

We also ran microcanonical ensemble (NVE) trajectories to measure dynamical quantities since coupling to a thermal bath, especially by the Andersen or Langevin thermostats provided in the AMBER codes, can perturb system dynamics. For each peptide-water model combination we ran thirty NVE trajectories of 20ns in length. Starting structures for these trajectories were selected from the 284K replica of each water model, separated by 1ns of replica exchange simulation to ensure structural decorrelation. Since only coordinate information (not velocity) was saved for the structural ensemble, structures were equilibrated at 284K for 100ps prior to the 20ns constant energy runs.

We use the *ptraj* module of AMBER to analyze the DSSP defined secondary structure[55], hydrogen-bonds and electrostatic/saltbridge interactions over the generated structural ensembles. We specify all possible donors and acceptors for the hydrogen bonds in our analysis. Default parameters are used for both hydrogen bond detection and DSSP in *ptraj*.

Simulation of NMR Experimental Observables

Using the SHIFTS[56-58] and SHIFTX[59] programs, we predict the chemical shifts for all protons and C_α and C_β carbon atoms by averaging these quantities over the members of the Boltzmann weighted simulation ensemble. The chemical shifts were also calculated on a population of "unstructured" conformations, defined as such if DSSP[55] did not identify any secondary structure category for any of the ten residues.

We also calculate the predicted scalar coupling constants $^3J_{HNH\alpha}$ by evaluating the ϕ dihedral angle for each member of the ensemble, calculating the instantaneous scalar coupling constant using the Karplus equation[60],

$$J(\varphi) = A\cos^2(\varphi - 60) + B\cos(\varphi - 60) + C \quad (1)$$

and collecting the average and standard deviation for $^3J_{HNH\alpha}$ for each residue. We used two types of parameter sets for A, B, and C in Eq. (1). The first type corresponds to fits of the Karplus equation using experimentally measured scalar coupling constants and a known reference protein structure; we explore the parameter set for $^3J_{HNH\alpha}$ given by Vuister and Bax where A = 6.51, B = -1.76 and C = 1.60[61], although other choices are possible[62-64]. In fact, it has been shown that variations between different Karplus parameterizations of Eq. (1) likely reflect differences in the average dihedral fluctuations about the reference equilibrium folded structure[62, 64]. Thus it is possible that if such parameters are used to generate <J> over the simulated ensembles, there will be a "double counting" of such motions. We

thus also considered a second parameter set in which a harmonic approximation to this dynamical motion has been removed, where A = 9.5, B = -1.4 and C = 0.30 [62].

To calculate the spectral density functions for ^{1}H-^{1}H spin pairs to predict ROESY data and for ^{13}C-^{1}H pairs to predict the relaxation parameters (T_1 and T_2), we follow the method of Peter et al.[65] in evaluating the following normalized time correlation function

$$C(\tau) = \left\langle \frac{1}{r^6(t)} \right\rangle^{-1} \left\langle \frac{P_2(\cos\chi_{t,t+\tau})}{r^3(t)r^3(t+\tau)} \right\rangle \tag{2}$$

where P_2 is the 2nd order Legendre polynomial, χ is the angle between the interspin vector in the laboratory reference frame connecting each of the ~1800 pairs of protons as well as the bonded C_α-H_α pairs at time t and $t+\tau$, $r(t)$ is the instantaneous pair distance, and the angle brackets denote a thermal average. We averaged over thirty independent constant energy (NVE) trajectories at 284K in evaluation of Eq. (2), for correlation times τ up to 5ns. We believe that using many trajectories run in parallel, launched with different representative members of the Boltzmann distribution of peptide conformations, is preferable to a single long trajectory in the NVE ensemble because it will not exhibit a canonical structural ensemble. Averaging multiple trajectories, each with a slightly different total energy, also has the minor added benefit of sampling the energy distribution of the canonical ensemble despite using constant energy trajectories. It is important to note that we "unnormalized" Eq. (2) by the $1/r^6$ average spin-spin distance in each trajectory in order to compute the average over trajectories.

Each resulting average numerical correlation function for a given atom pair is then fit to a triple exponential form using a shell script invoking the *fit* routine in Gnuplot. A triple exponential form was selected since multiple relaxation modes with different timescales invariably exist for a peptide. In our case, a very fast (<1ps) mode due to vibration and libration exists, as well as several reorientational modes arising from anisotropic tumbling due to the non-spherical shape of the peptide. Using a four exponential form did not show substantially different fits for a test group of data, and hence were not used. In some pair cases only two exponentials were required, although three exponential fits were typical.

The fitted time correlation function is then Fourier transformed to define the spectral density functions

$$J(\omega) = \int_{-\infty}^{\infty} C(\tau) e^{i\omega\tau} d\tau \tag{3}$$

where we use the following convention for the Fourier transform of an exponential

$$\int_{-\infty}^{\infty} e^{-\tau/b} e^{i\omega\tau} d\tau = \frac{2b}{1+\omega^2 b^2} \tag{3a}$$

and the appropriately chosen constant factors in Eqs. (3d-4c). We note that the peptide tumbles and locally reorients rapidly enough for all relevant spin-spin vector time-correlation functions approach zero within the time of our 20ns dynamics simulations.

The quantities in Eq. (2) and (3) allow us to define the T_1 and T_2 relaxation at the relevant ^{1}H and ^{13}C Larmor frequencies[49]. T_1 is defined as the inverse of the spin-lattice relaxation rate

$$R_1 = \frac{1}{T_1} = R_1^{DD} + R_1^{CSA} \tag{3b}$$

where R_1^{DD} and R_1^{CSA} are the dipolar and chemical shift anisotropy (CSA) components of the spin-lattice relaxation rate constants. T_2 is defined as the inverse of the spin-spin relaxation rate

$$R_2 = \frac{1}{T_2} = R_2^{DD} + R_2^{CSA} + R_a \tag{3c}$$

where R_2^{DD} and R_2^{CSA} are the dipolar and CSA components of the spin-spin relaxation rate constants and R_a is the sum of the relaxation rate constants for pseudo-first order processes such as chemical exchange and diffusion which we ignore for this analysis. The dipolar relaxation rates

$$R_1^{DD} = (1/20)K^2[J(\omega_H - \omega_C) + 3J(\omega_C) + 6J(\omega_H + \omega_C)] \tag{3d}$$

$$R_2^{DD} = (1/40)K^2[4J(0) + J(\omega_H - \omega_C) + 3J(\omega_C) + 3J(\omega_H) + 6J(\omega_H + \omega_C)] \tag{3e}$$

are the main contributors to the overall relaxation. The constant factor K is defined as

$$K = \frac{\mu_0}{4\pi\, r_{eff}^3} \hbar \gamma_a \gamma_b \tag{3f}$$

where μ_0 is the permeability of free space, $\hbar$ is Planck's constant, and γ_a and γ_b are the gyromagnetic ratios for the nuclei of interest which for the ^{13}C relaxation experiment are carbon and hydrogen, and r_{eff}

$$r_{eff} = \left\langle \frac{1}{r^6(t)} \right\rangle^{-1/6} \tag{3g}$$

is the appropriately averaged internuclear distance between atoms.

The chemical shift anisotropy contributions to the spin-lattice and spin-spin relaxation rates are incorporated in our T_1 and T_2 predictions by assuming an axially symmetric chemical shift tensor with chemical shift tensor parallel and perpendicular component difference, $\Delta\delta$, equal to 25ppm[49].

$$R_1^{\mathrm{CSA}} = (1/5)\Delta\delta^2\omega_{\mathrm{C}}{}^2 J(\omega_{\mathrm{C}}) \tag{3h}$$

$$R_2^{\mathrm{CSA}} = (1/5)(\Delta\delta^2\omega_{\mathrm{C}}{}^2/6)[4J(0) + 3J(\omega_{\mathrm{C}})] \tag{3i}$$

We can explicitly calculate the full time correlation functions and analytically FT these fits, and hence do not need to fit our spectral density functions through a Lipari-Szabo model-free analysis[66, 67] which has limited applicability when the system of interest lacks the separation of internal and external motion timescales, as is the case for $A\beta_{21\text{-}30}$. In order to compare our simulated T_1 and T_2 relaxation times to the experiment performed in ^2H_2O, we scale our time correlation functions by a factor of 1.2 as a simple approximation for the larger viscosity of ^2H_2O compared to H_2O at 10°C.

We also predict the ROESY spectra from our structural ensemble and dynamical trajectories by calculating the intensity

$$I(t_{\mathrm{mix}}) = Xe^{-\Lambda t_{\mathrm{mix}}} X^{-1} I(0) \tag{4a}$$

where X and Λ are the eigenvectors and eigenvalues of the full relaxation matrix, R, composed of the diagonal elements

$$\rho_{ii} = \sum_{j=1,\neq i}^{n} \frac{1}{10} K^2 \left[\frac{3}{2} J_{ij}(2\omega_0) + \frac{9}{4} J_{ij}(\omega_0) + \frac{5}{4} J_{ij}(0) \right] \tag{4b}$$

and off-diagonal elements

$$\sigma_{ij} = \frac{1}{10} K^2 \left[\frac{3}{2} J_{ij}(\omega_0) + J_{ij}(0) \right] \tag{4c}$$

where ρ is the direct dipolar relaxation rate and σ is the cross-relaxation rate for all proton pairs as described by van Gunsteren and coworkers[65, 68] and K is defined as above, with $\gamma_a\gamma_b$ equal to $\gamma_H{}^2$. Unlike the extended atom model (no aliphatic hydrogens) of these previous studies, we simulate all hydrogen atoms explicitly for each methyl group and hence calculate all pair correlation functions, including neighboring methylene and methyl group protons. We ignore water proton coordinates as is the standard assumption in the NMR experiment.

We solve this coupled system of differential equations for the magnetization matrix at the mixing time used by the NMR experiments for both H_2O and ^2H_2O. We simulate the experimental conditions of heavy water solvation on the relaxation matrix by removing the exchangeable hydrogens including backbone amides (HN), hydrogens in basic NH_3^+ groups, and hydroxyl hydrogens (HO) from the spin-matrix which we accomplished by setting all pair distances with these protons to 30Å. In order to generate peak predictions, we sum the peak volume contributions (including positive contributions

from cross peaks dominated by spin diffusion) for degenerate spins (methyl groups) as well as those from spins within the same residue that are indistinguishable at the resolution of our NMR experiments. We note that this method explicitly accounts for peak intensity effects caused by methyl group rotation since spectral density functions are calculated for each proton in a methyl group and the individual intensities from indistinguishable peaks are summed to compare to experimental spectra. Amine peak volumes in the H_2O spectra are scaled by a factor of 0.9 to approximately account for the presence of 10% deuterium exchanged amide protons from the 10% ^2H_2O used for NMR lock. Predicted cross peaks to basic amine and hydroxyl groups are filtered from the predictions since these cross peaks would be significantly broadened by exchange with solvent protons on the NMR timescale.

In order to directly compare simulations to experiment, we must determine the constant relating the arbitrary experimental cross peak intensity scale to the simulated intensities for diagonal magnetization of unity at mixing time of 0 ms. This is especially important since the experimental noise level must be determined to evaluate the ability of the predictions to separate observed and unobserved peaks. The constant relating the simulation and experimental scales is calculated by determining the slope of least-squares fit line (constrained to pass through the origin)[69] for the experimental intensities vs. simulated cross peak volumes of all cross peaks for all distinguishable pairs separated by four or more bonds, including all long range, medium range, and sequential peaks, as well as distant intra-residue pairs. We eliminate cross peaks between pairs separated by fewer bonds since they are subject to significant TOCSY intensity contributions, evident from lineshape distortion. All remaining experimental cross peak intensities (peak height) are assumed to be proportional to the volume, which assumes no significant lineshape distortion. This procedure was repeated for the two water model simulations, and for the two experimental solvation conditions (H_2O and ^2H_2O). The derived constant, multiplied by the weakest experimentally assigned peak intensity for the appropriate H_2O and ^2H_2O experiment, then provides an estimate of the noise level in the simulation. In the Results, the simulated and experimental intensities are now comparable as a multiplicative factor of the noise.

RESULTS

Chemical shifts

A robust chemical shift calculation must describe the anisotropic shielding of the applied magnetic field for the given atom, a quantity that depends sensitively on the local electronic structure environment. Even for folded proteins with a dominant native conformer, each atom type can exist in

many different local environments, making an accurate calculation of chemical shifts for a protein quite a challenge. This problem is exacerbated in the case of disordered proteins that have a far greater diversity of conformations and hence environments, hence empirical chemical shift packages that perform well for globular proteins such as SHIFTS[56-58] and SHIFTX[59] may inadequately predict chemical shifts of disordered proteins.

In Figure 1 we show the C_α, C_β, H_α and H_N experimental chemical shifts for $A\beta_{21-30}$ as compared to the calculated chemical shifts over our simulated ensemble for different force fields. For the experimental chemical shift values we subtracted the reference value of the chemical shift of a random coil at 25°C from the average shift for each amino acid[70]; while the carbon shifts show a very weak dependence on temperature and the 25°C random coil reference shift is used, the amide proton random coil shift reference for each amino acid is adjusted to a value appropriate for 10°C [71]. Together the chemical shift data emphasize that the peptide is largely unstructured.

In order to take into account any anticipated limitations of the calculations of the chemical shift theory, we calculate the average chemical shifts of our unstructured population, which comprises ~60% of the TIP4P-Ew and ~40% of the TIP3P ensemble. We then use these values as a random coil reference state that is subtracted from the total simulated ensemble with the hope of some cancellation of errors. Figure 1 shows that the resulting ensemble averaged chemical shifts calculated with SHIFTS show at best qualitative agreement with experiment for only the C_β shifts. The same calculation performed with SHIFTX shows similar results. While the calculated carbon and proton shift values deviate significantly from the NMR values, this may be due to the inability of the theory to capture all of the chemically relevant contributions to these chemical shifts, a notorious problem[56], as opposed to inadequacy of the structural ensemble, which we judge later from the calculation of other NMR observables.

Scalar coupling measurements

In Figure 2, we compare the $^3J_{H^NH\alpha}$ scalar coupling constants, measured from a high resolution COSY spectrum, to the simulations using the dynamically uncorrected and harmonically corrected Karplus parameters (see Methods). It is apparent that the dynamically uncorrected and harmonically corrected Karplus parameter sets work equally well on this disordered system (Figure 2a). This is because disordered systems, with the greater likelihood that all dihedral angles sample a much larger range of ϕ values, more closely approach the uniform sampling limit of $J = A/2+C$. This limit is very

similar between very different Karplus parameter sets, and for the sets examined here are 4.9Hz and 5.05Hz for the corrected and uncorrected sets, respectively.

However the use of dynamical corrections to the Karplus equation appears to be more theoretically sound[62, 64] and we apply this in Figure 2b. This figure shows that the TIP3P and TIP4P-Ew simulations have well converged average scalar coupling values between their two trajectories, and the two different water models show only small differences, less than 1 Hz. The overall agreement between simulation and experiment is quite good, making clear that both are consistent with an ensemble that is largely random coil, consistent with the chemical shift data. This is especially clear when we compare the experimental $^{3}J_{H}N_{H}\alpha$ values to that calculated from a single structure based on incorporating all of the ROESY restraints (shown in Figure 6 and developed further below). However the simulations are close but nonetheless outside of experimental error bars for residues 23-25 and may suggest problems with the underlying structural ensembles. However this may also be due to limitations of the parameterization of Eq. (1), since the simulated structures come from an unrestrained thermodynamic ensemble incorporating motion for a disordered peptide system, categorically different from the minimized x-ray and NMR structures created from restraints that are used to derive parameterizations of the Karplus equation for proteins.

NMR Spin Relaxation

The experimental C_α spin-lattice and spin-spin relaxation times measured for the non-glycine positions of $A\beta_{21-30}$ are presented in Table 1. Since the chemical shifts for ^{13}C-^{1}H pairs for Glu22 and Lys28 overlap, T_1 and T_2 at these positions cannot be distinguished and the parameters are treated as an average of relaxation times at the two positions. Since the combined data for these positions fit well to a single exponential form, T_1 and T_2 relaxation times are similar for these positions. The experimentally determined relaxation parameters vary by a maximum of 25% for non-terminal residues positions, indicating that the peptide does not contain significantly stiffer and/or slower moving regions on average.

T_1 and T_2 calculated from simulations of the peptide solvated with TIP4P-Ew model water show excellent agreement with the experimental values (Table 1). Non-terminal amino acid relaxation times are within ±10% for both T_1 and T_2. Consistent with experiment, the terminal amino acids show significantly longer relaxation times (indicating faster motion) than non-terminal ones, although the simulated relaxation times are larger than the experimental values. The discrepancy is greatest for the C-terminal alanine, which may indicate that the simulations predict less structure in this region than in

the experiment, although viscosity differences at lower temperature in ^2H_2O may influence the dynamics. To test this hypothesis, a time scaled correlation function was used for all proton pairs to account for the larger solvent viscosity (see Methods). We find that the C-terminal T_1 and T_2 are now within 15% of the experimental values while the non-terminal relaxation parameters change by only a few percent (Table 1)

T_1 and T_2 relaxation times calculated from the TIP3P simulations result are ~1.8 times larger than experimentally observed, for both terminal and non-terminal positions. This overestimate of relaxation time is a result of the faster dynamics of peptide motion in the TIP3P solvent. To demonstrate this difference the averaged vector autocorrelation function for the $^{13}C_\alpha$ and H_α pair at the Val24 position for both the TIP3P and TIP4P-Ew simulation is presented in Figure 3. The TIP3P simulations result in time correlation functions with fitted decay parameters more than twice as fast as those of the TIP4P-Ew simulations. The faster peptide motion in TIP3P is likely a result of the unrealistically low viscosity (faster self-diffusion) properties of the TIP3P model, speeding up the peptide dynamics. In addition to our observation here for a disordered peptide system, the realistic viscosity of models such as TIP4P-Ew has also most recently been shown to be critical for direct calculation of NMR relaxation times of in globular proteins[72].

Experimental and Simulated ROESY Crosspeaks

The 2D ROESY experiments in 90% H_2O:10% ^2H_2O and100% ^2H_2O yielded a set of 155 assigned ROESY crosspeaks. Although the majority of the crosspeaks were for intra-residue (83) and sequential (44) pairs, 28 weak medium range ROE interactions were also detected. These medium range ROE crosspeaks comprise several i,i+2 and i,i+3 interactions and two extremely weak i,i+4 interactions; no longer range ROE crosspeaks are observed and no strong patterns of α-helical or β-sheet contacts are evident. Lazo *et al*. report a long-range i,i+8 Glu22 H_α to Ala30 HN cross-peak[22], and more recent work from the same group assigns the peak to an overlap of the original Glu22 H_α to Ala30 HN interaction and i,i+2 Lys28 H_α to Ala30 HN in spectra collected at 500MHz[35]. The observation of the long-range ROE is critical to their proposed NMR model, which is significantly collapsed. However, due to the higher resolution of the spectrum we have collected at 900 MHz, we interpret the cross peak to be solely attributed to the i,i+2 contact between Lys28 H_α and Ala30 HN, as shown in Figure 4a.

An additional set of long-range interactions between the Glu22 and Lys28 sidechains are reported by Lazo *et al*. In our higher field spectra, we are able to distinguish the small chemical shift

difference between HB3 Lys28 and HB2 Glu22 (Figure 4b). At lower field, these resonances would overlap very close to the limit of the resolution of the experiment and hence be difficult to distinguish. We thus see no evidence of true Glu22 to Lys28 ROE interactions and believe that the previously reported long range cross peaks between these residues are due to misassignment of peaks too close to distinguish at lower field.

The new spectra show that a majority of the medium range cross peaks suggest turn or partial collapse structure for residues 22 through 27, although medium-range interactions are also seen from Ala21 to Asp23 and Val24, indicating the peptide backbone is not simply extended in the N-terminal region. Two additional pairs of interactions are found in the C-terminal region between the side chain and H_α of Lys28 with the backbone of Ala30, as well as the methyl group (HB) of Ala30 with both HB methylene atoms of Asn27.

Predicted ROESY cross peaks from simulation were calculated for a 300 ms mixing time and compared to the cross peaks observed in the H_2O and ^2H_2O experimental spectra in Tables 2 and 3. Since medium and long range ROE interactions contain the most information about peptide structure, we focus only on these interactions and ignore intra residue and sequential interactions in our comparisons of simulations to experiment. The top-ranked intensities for the ROE cross peaks predicted to be above the noise level are tabulated along with the experimentally measured value; a dash indicates no cross peak was seen experimentally, or "<1.0" for a potential experimental cross peak so weak that it cannot reliably be definitely assigned. Because we have two independent replica exchange calculations for each water model, we can explicitly evaluate convergence of the ROESY cross peaks. Although the r^1 (linear) pair distance averages vary less than a few percent between the simulations and suggest good convergence, a small number of r^{-6} averaged pair distance vary by >30% and translate into noticeable changes in the corresponding peak volumes, and thus peak ranking. We therefore specifically highlight below the few cross peaks where the combined ensemble cross peak predictions do not make evident the significantly different predictions from the independent simulations for both TIP4P-Ew and TIP3P.

Tables 2 and 3 show that the TIP4P-Ew and TIP3P ensembles predict 12 and 14 of the experimentally assigned cross peaks, respectively, from the 900 MHz H_2O spectra, and 14 and 15, respectively, of the assigned cross peaks in the 800 MHz ^2H_2O experiment (note that there is redundancy of cross peaks between the two experiments so that there are only 28 distinct cross-peaks in total). The true positive cross peaks encompass i,i+2, i,i+3 and i,i+4 medium range cross peaks from across the entire peptide. Thus both TIP3P and TIP4P-Ew ensembles pick out the majority of the 28

experimentally observed medium-range ROE interactions from the 600 possible distinguishable medium and long-range interactions.

The predictions also show a number of “false positive” cross peaks *i.e.* cross peak predicted above the estimated noise level in the simulations that are not experimentally observed. In the TIP4P-Ew predictions, all of the false positive cross peaks, excepting one from the H_2O spectrum and four additional from the ^2H_2O spectrum, are i,i+2 or i,i+3 assignments that involve residues and regions of the chain that have other observed ROE interactions. This suggests that the simulations are bringing together the correct regions of the peptide and that these false positives are due to small differences in the detailed structural distances. In fact the r^{-6} distance averaging to estimate peak volumes is extremely sensitive to distance, such that changes of $2^{1/6}$ (~1.12) in distance can translate to a doubling of the calculated peak volume. In other words, false positive cross peaks predicted to be weak but still above the noise by our simulations may be just below the background noise in the experiment if the simulated distances are closer than in the experiment by only a factor of 1.12.

We therefore focus on false positives predicted more than a factor of 2 above the noise. In this case the differences in quality of the water models are revealed in that the TIP3P simulations have far too many false positives as strongly predicted cross peaks, suggesting a structural ensemble that is far more collapsed than observed experimentally. The TIP3P model shows far more false positives above the estimated noise, and poor ranking for what are the strongest experimentally observed peaks. By contrast TIP4P-Ew has fewer false positives and gets the intensity rankings right for the most prominent experimental peaks. In fact, the TIP4P-Ew simulations of the cross peak of strongest intensity between the HB methyl group of Ala21 and the HG methyl groups of Val24 led to the assignment of this peak in the experimental spectra which was initially hidden beneath an experimental artifact. Therefore we focus on the TIP4P-Ew results in the remainder of the Results.

The more significant discrepancies between the experiments and simulation involve “false negatives”- experimentally observed cross peaks that are not predicted to be observable by simulation. Since the noise in the experiment is not uniform over the spectra, if we dip just below the estimate for noise by a factor of 2, the TIP4P-Ew simulation predictions show an additional four H_2O and two ^2H_2O experimentally assigned crosspeaks. Based on the highly sensitive cross peak intensity discussed above, we could thus classify these as true positives as well. However, five additional missing crosspeaks are a full factor of 10 below the noise level, and hence are genuine false negatives. One such set of false negatives are the interactions between β methylene protons of Asp 23 and Ser 26, which involve four cross peaks seen experimentally. Since one of the possible four cross peaks of

methylene pair interactions for these two residues is predicted among the top 10 of the ^2H_2O cross peaks predicted by the TIP4P-Ew simulations, it is apparent that the simulation is bringing together the correct areas of the side-chains, but not the correct detailed geometry in this region. Apparently the structure of the turn that is stabilized by the Asp23-Ser26 sidechain contacts favors the proximity of a single proton in a β-methylene pair, instead of the four possible contacts between pairs seen experimentally.

The experimental cross peaks, however, may imply more equivalent distances than are actually present in the underlying structural ensemble. Magnetization selectively ROE transferred through space to a single hydrogen in a methylene pair would subsequently be more evenly redistributed between the pair due to TOCSY type (through bond) transfer. TOCSY transfer is created by the rotating frame pulse during ROESY mixing, is difficult to remove completely[45], and is an effect that is not accounted for by the predicted ROESY spectra. These same arguments apply to the β methylene protons of Asn 27 and Ala 30, which involve four cross peaks seen experimentally, while the simulations find 1 of the crosspeaks above the noise and 2 crosspeaks just below the noise. The missing crosspeak between protons is too spatially distant in the simulated ensemble suggesting either that the simulations have imperfect local geometry or that selectively ROE transferred magnetization has been redistributed through TOCSY type transfer among methylene protons.

Peptide structure from experiments and simulations

Determining a single structure from multiple weak, medium range ROE experimental crosspeaks for disordered peptides can be misleading since it also possible that ROE crosspeaks arise from multiple distinct populations or perhaps a fully heterogeneous structural ensemble. Typical structure calculations on structured proteins assume that weak NOE or ROE cross peaks correspond to large (~4.5-6.0Å) upper distance restraints on a single well-defined structural population, and hence all the restraints should be applied simultaneously. Though we will show that the peptide ensemble involves significant disorder and hence it is inappropriate to use the standard structure determination methods[73-75], we calculate a single best-fit structure for purposes of comparison.

The set of restraints was used to calculate 1000 structures of $A\beta_{21-30}$ and the 50 lowest energy structures were aligned. For the entire peptide, the superposition of the final 50 structures has an RMSD of 0.81 ± 0.42 Å for the backbone atoms and 1.15 ± 0.61 Å for all heavy atoms. Sixteen of the twenty structures are within 1.0Å RMSD for all heavy atoms, forming the dominant cluster whose

lowest energy structure has three major bends, pinching together Asp23 to the Ser26, Gly25 to Lys28 and Asn27 to Ala30 (Figure 5). These bends are created by 12 unique (i, i+3) and (i,i+4) ROE interactions between residues Asp23-Ser26, Val24-Asn27, Val24-Lys28, Asp23-Ser26, Val24-Asn27, Val24-Lys28, Gly25-Lys28 and Asn27-Ala30.

Many of the crosspeaks for these interactions are very weak and detectable in the ROESY spectrum only when the peptide is dissolved in 100% $^{2}H_2O$, and there is only one cross peak between Gly25 HAs and Lys28 HDs detected. As a result, one of the three bends in the minimized structure backbone is stabilized by one backbone hydrogen bond, and a second by a single Lys28 NH_3^+ interaction, but most of the pair distances for which ROE interactions are observed are not restrained by any favorable intermolecular interactions. This lack of stabilizing interactions was also evident for the minimized structures for the $A\beta_{21\text{-}30}$ peptide model proposed previously by Lazo et al[22].

Given the good quality of the TIP4P-Ew simulated experimental observables presented above, we can refine the experimental picture by analyzing the underlying simulated ensemble for structural populations. Standard clustering by RMSD is not informative due to the lack of order in much of the ensemble. The two first principal components in a PCA analysis yielded only a single large population, giving little information about the underlying structure. Since hydrophobic collapse is unlikely to be the dominant structuring force in a peptide that has only a single large aliphatic and no aromatic residues, hydrogen bond interactions are hypothesized to stabilize the structure that gives rise to the ROE interactions. Thus the most useful tool for partitioning the structures is the patterning of the hydrogen bonding and electrostatic interactions that may persist in sub-populations. It is important to emphasize that 60-65% of the TIP4P-Ew population is unstructured by these metrics, however the remaining 35-40% of the population does explain the presence of the medium-range restraints observed in the experimental ROESY crosspeaks with a large degree of success.

In the TIP4P-Ew simulations, the most populated hydrogen-bond is between the sidechain carboxyl oxygens of Asp23 and the backbone amide of G25 (Figure 6a). This interaction is found in 17% of the ensemble, and stabilizes the backbone dihedral angles near to those of a type I β-turn for residues Asp23 to Ser26. A true type I β-turn, which is found in 5% of the population (Figure 6b), is defined by backbone hydrogen bonding between the backbone carbonyl oxygen of residue *i* (Asp23) with the backbone amide hydrogen of residue *i+3* (Ser26), resulting in the amide hydrogen of *i+2* (Gly25) pointing toward the sidechain of *i*, precisely this most populated hydrogen bond we found.

The peptide maintains a conformation near a type I β-turn if interactions between the carboxyl oxygens of Asp23 to the sidechain hydroxyl of Ser26 are found, consistent with the observed ROEs

which brings together the sidechain hydrogens of Asp23 and Ser26. If structures with at least one of these Asp23 to Ser26 interactions are also considered, the type I β-turn population increases from 5% to 14% of the ensemble, much higher than any other turn region in the peptide. While the TIP3P structural ensemble shows this turn in approximately 35% of the ensemble, its overrepresentation in the structured population most likely contributes to the poor agreement of ROE cross peak volumes when compared to experiment.

Despite the prevalence of structures with type I β-turn structure, the β-turn does not nucleate a β-sheet, which would be characterized by backbone contacts between Glu22 and Asn27. Instead, in the structures observed, the backbone amide of Asn27 hydrogen bonds to the backbone carbonyl oxygen of Asp23, precluding the formation of β-sheet structure. Furthermore, this interaction brings the Val24 methyl hydrogens near the Asn27 sidechain hydrogens, accounting for those observed ROE interactions. Other smaller groups of covarying hydrogen bonds are observed, including simultaneous interactions between the backbone carbonyl of Val24 with the backbone amide of both Asn27 and Lys28, bringing in proximity the Val24 sidechain with Asn27 sidechain as observed in the ROESY spectra.

Salt bridge formation between Asp23 and Lys28, observed in the solid state NMR structure of the $A\beta_{1-40}$ fibril, is found in 7% of the ensemble (Figure 7), while the competing salt bridge between Glu22 and Lys28 is found 1.5% of the time. Together these salt bridge structures are observed with comparable frequency to the turn populations, but the salt-bridge contacts do not stabilize either hydrogen bonding structure or close proximity of other protons in the intervening region. In principle a close contact involving the basic lysine amine hydrogens may be observed in a ROESY spectrum, but salt bridges, unless stable enough to prevent proton exchange at neutral pH of the basic amine on the NMR experiment timescale as in folded proteins, do not typically bring together NMR visible protons.

DISCUSSION

According to the high field NMR experiments, $A\beta_{21-30}$ shows no long-range and only weak medium-range ROE interactions, demonstrating none of the features of a protein with a single native state. We therefore conclude that the presence of a singly populated collapsed structure incorporating a unique bend due to a i,i+8 Glu22 H_α to Ala30 HN crosspeak and i,i+6 Glu22 sidechain to Lys28 sidechain crosspeak reported by Lazo *et al.* and Grant *et al*. is incorrect on two levels. The first is a problem of misassignment in their lower resolution ROESY spectra in which they propose a i,i+8 interaction that is instead revealed to be a weak i,i+2 interaction and a i,i+6 interaction where intra-

residue peaks are overlapping, both of which we were able to distinguish by the higher resolution 800 and 900 MHz spectra used here.

More significantly, peptides and disordered protein systems should not conform to a single dominant structure, and should only be described by appropriate ensembles. The poor quality of a single structure becomes evident when simultaneously applying all ROE interactions as distance restraints to give a minimized structure with surprisingly few favorable inter-residue interactions. Since there are only a few restraints that are all "weak" and hence provide only a loose upper bound on the distance, all of the restraints are satisfied by pair distances near this bound. This loose bounding results in a dominant structure with no consensus stabilizing contacts, hydrogen bonds, regular secondary structures or reverse turns.

We determined a good match between the TIP4P-Ew/ff99SB simulated and experimentally observed structure and dynamics, as measured by ROE cross peaks and ^{13}C relaxation, indicating that these simulations faithfully approximate the ensemble of structures interrogated by the experiments, allowing them to be used to describe the full structural ensemble diversity. We find that the structural ensemble of the $A\beta_{21-30}$ involves a majority (~60%) of unstructured population according to lack of any DSSP secondary structure assignment or hydrogen-bonding patterns. However, the remaining minority population involves ~14% population of β-turn structure centered at Val24 and G25 bringing together Asp23 and S26. The simulations also indicate that the Asp23 to Lys28 salt bridge, important to the fibril structure, is formed in ~7% of the ensemble. Finally a separate set of structures populated only by a few percent brings together the Val24 and Asn27 regions. We emphasize however that the $A\beta_{21-30}$ system is highly disordered, and that the ~5-15% of distinct structural populations we measure have been overrepresented in all previous experimental and most simulation studies on this same system. Experimental and simulation data suggest that the structural populations may increase upon lengthening of the Aβ peptide to larger fragments[85-88].

CONCLUSION

Although significant progress has been made recently in the interpretation of NMR observables for disordered peptide and protein systems[76-79] combining multiple and independent structural constraints for a system with significant disorder often leads to an inadequate description of the ensemble diversity[77]. By contrast molecular dynamics simulations of disordered systems has the opposite challenge where the simulated ensemble is directly observable with good statistical confidence but the accuracy is difficult to assess due to incomplete convergence and uncertainties of

the underlying empirical force fields[80, 81]. While simulations of folded proteins in their native state have been shown to quantitatively reproduce NMR observables (model-free order parameters, relaxation times T_1 and T_2) [40, 82, 83], partially structured peptides and natively unfolded proteins present a new challenge for simulations in which small energetic biases or inaccuracies can dramatically affect the populations of structures in the equilibrium ensemble. Stock, Schwalbe and coworkers have recently shown that many earlier generation peptide-water empirical force field combinations simply do not reproduce the average structural ensemble for a simple disordered system such as polyalanine[84].

The recent advent of improved empirical force fields, enhanced sampling techniques, and NMR relaxation matrix calculations have allowed us to predict well the high quality NMR experimental observables generated here. The Amber ff99SB/TIP4P-Ew simulations do not over predict contacts between regions where there are no experimentally observed ROEs and thus there are few false positive peaks, while false negatives are weak but often just buried in the noise. By contrast, the TIP3P simulations involve structural ensembles that are too collapsed, resulting in far too strong, and far too many (false positive) ROE cross peaks. Additionally, the solution dynamics are much too fast to correctly reproduce the observed ^{13}C relaxation times. It would be instructive to see if the previous calculations on polyalanine might improve with the newer water force field.

At the same time the experimental and predicted observables do not match perfectly for ff99SB/TIP4P-EW, and the reasons for the discrepancy vary. We used two different chemical shift programs SHIFTS[56-58] and SHIFTX[59] (parameters derived from a physical vs. a statistical approach), and largely found the same level of disagreement with the experimental chemical shifts. We believe that the poor agreement of the calculated chemical shifts is inherent in the underlying chemical shift parameterizations that are optimized for folded states, as opposed to gross deficiencies of the underlying structural ensembles of the disordered peptide studied here. While comparisons to scalar coupling constants $^3J_{HNH\alpha}$ are overall very good, there are some discrepancies between simulation and experiment for residues 23-25. While the simulated ensembles may be imperfect, it also seems likely that use of Karplus parameters derived from minimized x-ray and NMR structures created from restraints may in fact be non-optimal when applied to an unrestrained thermodynamic ensemble for a disordered peptide or protein system. For ROESY spectra, the severity of r^{-6} averaging means that slight average distance changes can have greater than two-fold effects on the peak volume; therefore, regions of the chain correctly brought together in close proximity may emphasize local geometric rotomers that are imperfectly captured by the empirical force fields. Potential experimental artifacts such as through-bond TOCSY transfer mechanisms which

are not taken into account in the back calculation of ROESY cross-peaks may additionally contribute to prediction and experiment discrepancies. All of these issues are worthy of consideration for future improvements in next generation force fields and simulation of NMR observables. Even so, these structural and dynamical predictions match better than any previous predictions for peptides of this length range, a success that we attribute in particular to the advent of new generation force fields and careful verification that ensembles are adequately converged.

Faithfully predicting NOESY or ROESY cross peaks is challenging since the nature of the Overhauser effect singles out the minority populations of close range interactions (if they exist) through a steep power dependence on distance, making them both more structurally informative but much harder to converge in the simulated equilibrium ensemble. By contrast, each member of the structural ensemble contributes equally to averaged quantities such as chemical shift and scalar coupling observables, making prediction of these quantities from simulations much easier to converge, but far less structurally informative. If we were only to have examined the chemical shift and scalar coupling ($^{3}J_{HNH\alpha}$) measures, we would have found that either the TIP3P or the TIP4P-Ew solvated ff99SB peptide would have equivalently reproduced the experimental data. For a small and disordered peptide that exchanges conformations on timescales faster than the experimental timescale, the scalar coupling and chemical shift values provide direct Boltzmann weighted information dominated by the significant percentage of “random coil” structure. Conversely, predicted ROE interactions are sensitive to minor populations of close contacts that distinguish a true partially structured ensemble from other partially structured, or even completely unstructured, ensembles. Predicting the ROE interactions is therefore a more stringent test for simulations which must distinguish a smaller population of heterogeneous structure from a high percentage background of unstructured or random coil like structure in the ensemble.

We believe that the interplay of molecular simulation in reproducing a variety of NMR observables such as chemical shifts, scalar couplings, NOE or ROE cross peaks, and ^{13}C relaxations provides the correct tools for characterizing the structural ensemble for disordered systems. We note that proteolysis experiments, which implied well protected structure for the $A\beta_{21-30}$ fragment and the full length $A\beta_{1-40}$ and $A\beta_{1-42}$ sequences, appears to be an insensitive tool to distinguish a largely disordered ensemble from a highly folded population, at least in this case. As such this work serves as a validation study for ROESY characterization of $A\beta_{1-40}$ and $A\beta_{1-42}$ by molecular simulation, where collection of detailed NMR data will be more challenging due to aggregation and fibril formation on experimental timescales at physiological conditions.

ACKNOWLEDGEMENTS. We thank Dr. Jeff Pelton and the Central California 900 MHz Facility (supported under NIH-GM68933) for experimental resources and assistance. We thank the NSF Cyberinfrastructure program for support of the computational work presented here. We also acknowledge the National Energy Research Scientific Computing Center (supported by the Office of Science of the U.S. Department of Energy under Contract No. DE-AC03-76SF00098) and the Seaborg reimbursement program and Marvin Stodolsky for the needed cycles.

REFERENCES

1. Goedert, M.; Spillantini, M. G., A century of Alzheimer's disease. *Science* **2006,** 314, (5800), 777-781.
2. Dobson, C. M., Principles of protein folding, misfolding and aggregation. *Semin Cell Dev Biol* **2004,** 15, (1), 3-16.
3. Petkova, A. T.; Leapman, R. D.; Guo, Z. H.; Yau, W. M.; Mattson, M. P.; Tycko, R., Self-propagating, molecular-level polymorphism in Alzheimer's beta-amyloid fibrils. *Science* **2005,** 307, (5707), 262-265.
4. Bucciantini, M.; Giannoni, E.; Chiti, F.; Baroni, F.; Formigli, L.; Zurdo, J. S.; Taddei, N.; Ramponi, G.; Dobson, C. M.; Stefani, M., Inherent toxicity of aggregates implies a common mechanism for protein misfolding diseases. *Nature* **2002,** 416, (6880), 507-511.
5. Bucciantini, M.; Calloni, G.; Chiti, F.; Formigli, L.; Nosi, D.; Dobson, C. M.; Stefani, M., Prefibrillar amyloid protein aggregates share common features of cytotoxicity. *Journal of Biological Chemistry* **2004,** 279, (30), 31374-31382.
6. Stefani, M.; Dobson, C. M., Protein aggregation and aggregate toxicity: new insights into protein folding, misfolding diseases and biological evolution. *Journal of Molecular Medicine-Jmm* **2003,** 81, (11), 678-699.
7. Braak, H.; Braak, E., Evolution of neuronal changes in the course of Alzheimer's disease. *Journal of Neural Transmission-Supplement* **1998**, (53), 127-140.
8. Lambert, M. P.; Barlow, A. K.; Chromy, B. A.; Edwards, C.; Freed, R.; Liosatos, M.; Morgan, T. E.; Rozovsky, I.; Trommer, B.; Viola, K. L.; Wals, P.; Zhang, C.; Finch, C. E.; Krafft, G. A.; Klein, W. L., Diffusible, nonfibrillar ligands derived from A beta(1-42) are potent central nervous system neurotoxins. *Proceedings of the National Academy of Sciences of the United States of America* **1998,** 95, (11), 6448-6453.
9. Stine, W. B.; Dahlgren, K. N.; Krafft, G. A.; LaDu, M. J., In vitro characterization of conditions for amyloid-beta peptide oligomerization and fibrillogenesis. *Journal of Biological Chemistry* **2003,** 278, (13), 11612-11622.
10. Balbach, J. J.; Petkova, A. T.; Oyler, N. A.; Antzutkin, O. N.; Gordon, D. J.; Meredith, S. C.; Tycko, R., Supramolecular structure in full-length Alzheimer's beta-amyloid fibrils: Evidence for a parallel beta-sheet organization from solid-state nuclear magnetic resonance. *Biophysical Journal* **2002,** 83, (2), 1205-1216.
11. Petkova, A. T.; Ishii, Y.; Balbach, J. J.; Antzutkin, O. N.; Leapman, R. D.; Delaglio, F.; Tycko, R., A structural model for Alzheimer's beta-amyloid fibrils based on experimental constraints from solid state NMR. *Proceedings of the National Academy of Sciences of the United States of America* **2002,** 99, (26), 16742-16747.

12. Petkova, A. T.; Leapman, R. D.; Yau, W. M.; Tycko, R., Structural investigations of Alzheimer's beta-amyloid fibrils by solid state NMR. *Biophysical Journal* **2004,** 86, (1), 506A-506A.
13. Petkova, A. T.; Yau, W. M.; Tycko, R., Experimental constraints on quaternary structure in Alzheimer's beta-amyloid fibrils. *Biochemistry* **2006,** 45, (2), 498-512.
14. Tycko, R.; Petkova, A.; Oyler, N.; Chan, C. C.; Balbach, J., Probing the molecular structure of amyloid fibrils with solid state NMR. *Biophysical Journal* **2002,** 82, (1), 187A-187A.
15. Crescenzi, O.; Tomaselli, S.; Guerrini, R.; Salvadori, S.; D'Ursi, A. M.; Temussi, P. A.; Picone, D., Solution structure of the Alzheimer amyloid beta-peptide (1-42) in an apolar microenvironment. Similarity with a virus fusion domain. *Eur J Biochem* **2002,** 269, (22), 5642-8.
16. Coles, M.; Bicknell, W.; Watson, A. A.; Fairlie, D. P.; Craik, D. J., Solution structure of amyloid beta-peptide(1-40) in a water-micelle environment. Is the membrane-spanning domain where we think it is? *Biochemistry* **1998,** 37, (31), 11064-77.
17. Shao, H.; Jao, S.; Ma, K.; Zagorski, M. G., Solution structures of micelle-bound amyloid beta-(1-40) and beta-(1-42) peptides of Alzheimer's disease. *J Mol Biol* **1999,** 285, (2), 755-73.
18. Sticht, H.; Bayer, P.; Willbold, D.; Dames, S.; Hilbich, C.; Beyreuther, K.; Frank, R. W.; Rosch, P., Structure of amyloid A4-(1-40)-peptide of Alzheimer's disease. *Eur J Biochem* **1995,** 233, (1), 293-8.
19. Sgourakis, N. G.; Yan, Y.; McCallum, S. A.; Wang, C.; Garcia, A. E., The Alzheimer's peptides Abeta40 and 42 adopt distinct conformations in water: a combined MD / NMR study. *J Mol Biol* **2007,** 368, (5), 1448-57.
20. Yan, Y.; Liu, J.; McCallum, S. A.; Yang, D.; Wang, C., Methyl dynamics of the amyloid-beta peptides Abeta40 and Abeta42. *Biochem Biophys Res Commun* **2007,** 362, (2), 410-4.
21. Yan, Y.; Wang, C., Abeta42 is more rigid than Abeta40 at the C terminus: implications for Abeta aggregation and toxicity. *J Mol Biol* **2006,** 364, (5), 853-62.
22. Lazo, N. D.; Grant, M. A.; Condron, M. C.; Rigby, A. C.; Teplow, D. B., On the nucleation of amyloid beta-protein monomer folding. *Protein Sci* **2005,** 14, (6), 1581-96.
23. Sciarretta, K. L.; Gordon, D. J.; Petkova, A. T.; Tycko, R.; Meredith, S. C., A beta 40-Lactam(D23/K28) models a conformation highly favorable for nucleation of amyloid. *Biochemistry* **2005,** 44, (16), 6003-6014.
24. Grabowski, T. J.; Cho, H. S.; Vonsattel, J. P. G.; Rebeck, G. W.; Greenberg, S. M., Novel amyloid precursor protein mutation in an Iowa family with dementia and severe cerebral amyloid angiopathy. *Annals of Neurology* **2001,** 49, (6), 697-705.
25. Fawzi, N. L.; Kohlstedt, K. L.; Okabe, Y.; Head-Gordon, T., Protofibril Assemblies of the Arctic, Dutch and Flemish Mutants of the Alzheimer's A{beta}1-40 Peptide. *Biophys J* **2007**.
26. Hendriks, L.; Vanduijn, C. M.; Cras, P.; Cruts, M.; Vanhul, W.; Vanharskamp, F.; Warren, A.; McInnis, M. G.; Antonarakis, S. E.; Martin, J. J.; Hofman, A.; Vanbroeckhoven, C., Presenile-dementia and cerebral-hemorrhage linked to a mutation at codon-492 of the beta-amyloid precursor protein gene. *Nature Genetics* **1992,** 1, (3), 218-221.
27. Kamino, K.; Orr, H. T.; Payami, H.; Wijsman, E. M.; Alonso, M. E.; Pulst, S. M.; Anderson, L.; Odahl, S.; Nemens, E.; White, J. A.; Sadovnick, A. D.; Ball, M. J.; Kaye, J.; Warren, A.; McInnis, M.; Antonarakis, S. E.; Korenberg, J. R.; Sharma, V.; Kukull, W.; Larson, E.; Heston, L. L.; Martin, G. M.; Bird, T. D.; Schellenberg, G. D., Linkage and mutational analysis of familial Alzheimer-Disease kindreds for the APP gene region. *American Journal of Human Genetics* **1992,** 51, (5), 998-1014.
28. Walsh, D. M.; Hartley, D. M.; Condron, M. M.; Selkoe, D. J.; Teplow, D. B., In vitro studies of amyloid beta-protein fibril assembly and toxicity provide clues to the aetiology of Flemish variant (Ala(692) -> Gly) Alzheimer's disease. *Biochemical Journal* **2001,** 355, 869-877.

29. Levy, E.; Carman, M. D.; Fernandez-Madrid, I. J.; Power, M. D.; Lieberburg, I.; van Duinen, S. G.; Bots, G. T.; Luyendijk, W.; Frangione, B., Mutation of the Alzheimer's disease amyloid gene in hereditary cerebral hemorrhage, Dutch type. *Science* **1990,** 248, (4959), 1124-6.
30. Bugiani, O.; Padovani, A.; Magoni, M.; Andora, G.; Sgarzi, M.; Savoiardo, M.; Bizzi, A.; Giaccone, G.; Rossi, G.; Tagliavini, F., An Italian type of HCHWA. *Neurobiol Aging* **1998,** 19, S238.
31. Tagliavini, F.; Rossi, G.; Padovani, A.; Magoni, M.; Andora, G.; Sgarzi, M.; Bizzi, A.; Savoiardo, M.; Carella, F.; Morbin, M.; Giaccone, G.; Bugiani, O., A new betaPP mutation related to hereditary cerebral hemorrhage. *Alzheimer's reports: vascular factors in Alzheimer's disease* **1999,** 2, (Suppl1), S28.
32. Van Nostrand, W. E.; Melchor, J. P.; Keane, D. M.; Saporito-Irwin, S. M.; Romanov, G.; Davis, J.; Xu, F., Localization of a fibrillar amyloid beta-protein binding domain on its precursor. *Journal of Biological Chemistry* **2002,** 277, (39), 36392-36398.
33. Van Nostrand, W. E.; Melchor, J. P.; Romanov, G.; Zeigler, K.; Davis, J., Pathogenic effects of cerebral amyloid angiopathy mutations in the amyloid beta-protein precursor. In *Alzheimer's Disease: Vascular Etiology and Pathology*, New York Acad Sciences: New York, 2002; pp 258-265.
34. Nilsberth, C.; Westlind-Danielsson, A.; Eckman, C. B.; Condron, M. M.; Axelman, K.; Forsell, C.; Stenh, C.; Luthman, J.; Teplow, D. B.; Younkin, S. G.; Naslund, J.; Lannfelt, L., The 'Arctic' APP mutation (E693G) causes Alzheimer's disease by enhanced A beta protofibril formation. *Nature Neuroscience* **2001,** 4, (9), 887-893.
35. Grant, M. A.; Lazo, N. D.; Lomakin, A.; Condron, M. M.; Arai, H.; Yamin, G.; Rigby, A. C.; Teplow, D. B., Familial Alzheimer's disease mutations alter the stability of the amyloid beta-protein monomer folding nucleus. *Proc Natl Acad Sci U S A* **2007,** 104, (42), 16522-7.
36. Baumketner, A.; Bernstein, S. L.; Wyttenbach, T.; Lazo, N. D.; Teplow, D. B.; Bowers, M. T.; Shea, J. E., Structure of the 21-30 fragment of amyloid beta-protein. *Protein Sci* **2006,** 15, (6), 1239-47.
37. Borreguero, J. M.; Urbanc, B.; Lazo, N. D.; Buldyrev, S. V.; Teplow, D. B.; Stanley, H. E., Folding events in the 21-30 region of amyloid beta-protein (Abeta) studied in silico. *Proc Natl Acad Sci U S A* **2005,** 102, (17), 6015-20.
38. Cruz, L.; Urbanc, B.; Borreguero, J. M.; Lazo, N. D.; Teplow, D. B.; Stanley, H. E., Solvent and mutation effects on the nucleation of amyloid beta-protein folding. *Proc Natl Acad Sci USA* **2005,** 102, (51), 18258-63.
39. Chen, W.; Mousseau, N.; Derreumaux, P., The conformations of the amyloid-beta (21-30) fragment can be described by three families in solution. *J Chem Phys* **2006,** 125, (8), 084911.
40. Hornak, V.; Abel, R.; Okur, A.; Strockbine, B.; Roitberg, A.; Simmerling, C., Comparison of multiple Amber force fields and development of improved protein backbone parameters. *Proteins* **2006,** 65, (3), 712-25.
41. Horn, H. W.; Swope, W. C.; Pitera, J. W.; Madura, J. D.; Dick, T. J.; Hura, G. L.; Head-Gordon, T., Development of an improved four-site water model for biomolecular simulations: TIP4P-Ew. *J Chem Phys* **2004,** 120, (20), 9665-78.
42. Delaglio, F.; Grzesiek, S.; Vuister, G. W.; Zhu, G.; Pfeifer, J.; Bax, A., NMRPipe: a multidimensional spectral processing system based on UNIX pipes. *J Biomol NMR* **1995,** 6, (3), 277-93.
43. Johnson, B. A.; Blevins, R. A.; Pe, NMR VIEW - A computer-program for the visualization and analysis of NMR data. *Journal of Biomolecular NMR* **1994,** 4, (5), 603-614.
44. Keller, R., *The Computer Aided Resonance Assignment Tutorial*. CANTINA Verlag: 2004.

45. Hwang, T. L.; Shaka, A. J.; Hm, Cross relaxation without TOCSY - Transverse rotating-frame Overhauser effect spectroscopy. *Journal of the American Chemical Society* **1992,** 114, (8), 3157-3159.
46. Guntert, P., Automated NMR structure calculation with CYANA. *Methods Mol Biol* **2004,** 278, 353-78.
47. DeLano, W. L., *The PyMOL Molecular Graphics System*. DeLano Scientific: San Carlos, CA, USA., 2002.
48. Case, D. A.; Cheatham, T. E., 3rd; Darden, T.; Gohlke, H.; Luo, R.; Merz, K. M., Jr.; Onufriev, A.; Simmerling, C.; Wang, B.; Woods, R. J., The Amber biomolecular simulation programs. *J Comput Chem* **2005,** 26, (16), 1668-88.
49. Palmer, A. G.; Rance, M.; Wright, P. E., Intramolecular Motions of a Zinc Finger DNA-Binding Domain from Xfin Characterized by Proton-Detected Natural Abundance C-13 Heteronuclear NMR Spectroscopy. *Journal of the American Chemical Society* **1991,** 113, (12), 4371-4380.
50. Jorgensen, W. L.; Chandrasekhar, J.; Madura, J. D.; Impey, R. W.; Klein, M. L., Comparison of Simple Potential Functions for Simulating Liquid Water. *Journal of Chemical Physics* **1983,** 79, (2), 926-935.
51. Andersen, H. C., Molecular-Dynamics Simulations at Constant Pressure and-or Temperature. *Journal of Chemical Physics* **1980,** 72, (4), 2384-2393.
52. Darden, T.; York, D.; Pedersen, L., Particle Mesh Ewald - an N.Log(N) Method for Ewald Sums in Large Systems. *Journal of Chemical Physics* **1993,** 98, (12), 10089-10092.
53. Hukushima, K.; Nemoto, K., Exchange Monte Carlo method and application to spin glass simulations. *Journal of the Physical Society of Japan* **1996,** 65, (6), 1604-1608.
54. Geyer, C. J.; Thompson, E. A., Annealing Markov-Chain Monte-Carlo with Applications to Ancestral Inference. *Journal of the American Statistical Association* **1995,** 90, (431), 909-920.
55. Kabsch, W.; Sander, C., Dictionary of protein secondary structure: pattern recognition of hydrogen-bonded and geometrical features. *Biopolymers* **1983,** 22, (12), 2577-637.
56. Moon, S.; Case, D. A., A new model for chemical shifts of amide hydrogens in proteins. *J Biomol NMR* **2007,** 38, (2), 139-50.
57. Xu, X. P.; Case, D. A., Automated prediction of 15N, 13Calpha, 13Cbeta and 13C' chemical shifts in proteins using a density functional database. *J Biomol NMR* **2001,** 21, (4), 321-33.
58. Osapay, K.; Case, D. A., Analysis of proton chemical shifts in regular secondary structure of proteins. *J Biomol NMR* **1994,** 4, (2), 215-30.
59. Neal, S.; Nip, A. M.; Zhang, H.; Wishart, D. S., Rapid and accurate calculation of protein 1H, 13C and 15N chemical shifts. *J Biomol NMR* **2003,** 26, (3), 215-40.
60. Karplus, M.; Grant, D. M., A Criterion For Orbital Hybridization And Charge Distribution In Chemical Bonds. *Proc Natl Acad Sci U S A* **1959,** 45, (8), 1269-73.
61. Vuister, G. W.; Bax, A., Quantitative J Correlation - a New Approach for Measuring Homonuclear 3-Bond J(H(N)H(Alpha) Coupling-Constants in N-15-Enriched Proteins. *Journal of the American Chemical Society* **1993,** 115, (17), 7772-7777.
62. Bruschweiler, R.; Case, D. A., Adding Harmonic Motion to the Karplus Relation for Spin-Spin Coupling. *J Am Chem Soc* **1994,** 116, (24), 11199-200.
63. Habeck, M.; Rieping, W.; Nilges, M., Bayesian estimation of Karplus parameters and torsion angles from three-bond scalar couplings constants. *J Magn Reson* **2005,** 177, (1), 160-5.
64. Lindorff-Larsen, K.; Best, R. B.; Vendruscolo, M., Interpreting dynamically-averaged scalar couplings in proteins. *J Biomol NMR* **2005,** 32, (4), 273-80.
65. Peter, C.; Daura, X.; van Gunsteren, W. F., Calculation of NMR-relaxation parameters for flexible molecules from molecular dynamics simulations. *J Biomol NMR* **2001,** 20, (4), 297-310.

66. Lipari, G.; Szabo, A., Model-Free Approach to the Interpretation of Nuclear Magnetic-Resonance Relaxation in Macromolecules.2. Analysis of Experimental Results. *Journal of the American Chemical Society* **1982,** 104, (17), 4559-4570.
67. Lipari, G.; Szabo, A., Model-Free Approach to the Interpretation of Nuclear Magnetic-Resonance Relaxation in Macromolecules.1. Theory and Range of Validity. *Journal of the American Chemical Society* **1982,** 104, (17), 4546-4559.
68. Daura, X.; Glattli, A.; Gee, P.; Peter, C.; van Gunsteren, W. F., Unfolded state of peptides. *Adv Protein Chem* **2002,** 62, 341-60.
69. Feenstra, K. A.; Peter, C.; Scheek, R. M.; van Gunsteren, W. F.; Mark, A. E., A comparison of methods for calculating NMR cross-relaxation rates (NOESY and ROESY intensities) in small peptides. *Journal of Biomolecular Nmr* **2002,** 23, (3), 181-194.
70. Wishart, D. S.; Bigam, C. G.; Yao, J.; Abildgaard, F.; Dyson, H. J.; Oldfield, E.; Markley, J. L.; Sykes, B. D., H-1, C-13 and N-15 Chemical-Shift Referencing in Biomolecular Nmr. *Journal of Biomolecular Nmr* **1995,** 6, (2), 135-140.
71. Merutka, G.; Dyson, H. J.; Wright, P. E., Random Coil H-1 Chemical-Shifts Obtained as a Function of Temperature and Trifluoroethanol Concentration for the Peptide Series Ggxgg. *Journal of Biomolecular Nmr* **1995,** 5, (1), 14-24.
72. Wong, V.; Case, D. A., Evaluating Rotational Diffusion from Protein MD Simulations. *J Phys Chem B* **2007**.
73. Nanzer, A. P.; van Gunsteren, W. F.; Torda, A. E., Parameterization of time-averaged distance restraints in MD simulations. *Journal of Biomolecular NMR* **1995,** 6, (3), 313-320.
74. Torda, A. E.; Scheek, R. M.; van Gunsteren, W. F., Time-averaged nuclear Overhauser effect distance restraints applied to tendamistat. *Journal of Molecular Biology* **1990,** 214, (1), 223-235.
75. Torda, A. E.; Scheek, R. M.; van Gunsteren, W. F., Time-dependent distance restraints in molecular-dynamics simulations. *Chemical Physics Letters* **1989,** 157, (4), 289-294.
76. Marsh, J. A.; Singh, V. K.; Jia, Z.; Forman-Kay, J. D., Sensitivity of secondary structure propensities to sequence differences between alpha- and gamma-synuclein: implications for fibrillation. *Protein Sci* **2006,** 15, (12), 2795-804.
77. Marsh, J. A.; Neale, C.; Jack, F. E.; Choy, W. Y.; Lee, A. Y.; Crowhurst, K. A.; Forman-Kay, J. D., Improved structural characterizations of the drkN SH3 domain unfolded state suggest a compact ensemble with native-like and non-native structure. *J Mol Biol* **2007,** 367, (5), 1494-510.
78. Choy, W. Y.; Forman-Kay, J. D., Calculation of ensembles of structures representing the unfolded state of an SH3 domain. *J Mol Biol* **2001,** 308, (5), 1011-32.
79. Bezsonova, I.; Evanics, F.; Marsh, J. A.; Forman-Kay, J. D.; Prosser, R. S., Oxygen as a paramagnetic probe of clustering and solvent exposure in folded and unfolded states of an SH3 domain. *J Am Chem Soc* **2007,** 129, (6), 1826-35.
80. Mu, Y. G.; Kosov, D. S.; Stock, G.; Zt, Conformational dynamics of trialanine in water. 2. Comparison of AMBER, CHARMM, GROMOS, and OPLS force fields to NMR and infrared experiments. *Journal of Physical Chemistry B* **2003,** 107, (21), 5064-5073.
81. Mu, Y. G.; Stock, G.; Uw, Conformational dynamics of trialanine in water: A molecular dynamics study. *Journal of Physical Chemistry B* **2002,** 106, (20), 5294-5301.
82. Case, D. A., Molecular dynamics and NMR spin relaxation in proteins. *Acc Chem Res* **2002,** 35, (6), 325-31.
83. Showalter, S. A.; Johnson, E.; Rance, M.; Bruschweiler, R., Toward quantitative interpretation of methyl side-chain dynamics from NMR by molecular dynamics simulations. *J Am Chem Soc* **2007**.

84. Graf, J.; Nguyen, P. H.; Stock, G.; Schwalbe, H., Structure and dynamics of the homologous series of alanine peptides: a joint molecular dynamics/NMR study. *J Am Chem Soc* **2007,** 129, (5), 1179-89.
85. Tarus, B.; Straub, J. E.; Thirumalai, D., Dynamics of Asp23-Lys28 salt-bridge formation in Aβ(10-35) monomers. *J Am Chem Soc* **2007**, 128, 16159-16168.
86. Massi, F.; Peng, J. W.; Lee, J. P.; Straub, J.E., Simulation study of the structure and dynamics of the Alzheimer's amyloid peptide congener in solution. *Biophys J.* **2001**, 80(1), 31–44.
87. Kirschner, D. A.; Inouye, H.; Duffy, L. K.; Sinclair, A.; Lind, M.; Selkoe, D. J., Synthetic peptide homologous to β protein from alzheimer disease forms amyloid-like fibrils in vitro. *Proc Natl Acad Sci USA* **1987**, 84, 6953-6957.
88. Barrow, C. J.; Yasuda, A.; Kenny, P. T.; Zagorski. M.G., Solution conformations and aggregational properties of synthetic amyloid beta-peptides of Alzheimer's disease. Analysis of circular dichroism spectra. *J. Mol. Biol.* **1992**, 225, 1075–1093.

FIGURES

Figure 1 *^{13}C and ^{1}H chemical shifts from experiment and simulation for $A\beta_{21\text{-}30}$.* Experimental NMR shifts are calculated as difference from the peptide measurements and tabulated random coil values. For *^{13}C*, which are insensitive to temperature changes, we used the tabulated 25°C random coil shifts, while for the amide proton shifts we used the random coil values of 10°C to account for the temperature used in this study. The predicted chemical shifts are SHIFTS calculations averaged over the full ensemble after subtracting SHIFTS calculations averaged over the unstructured subpopulations (as defined by lack of DSSP secondary structure for all residues to represent our calculated random coil population).

Figure 2. *Comparison of experimental scalar coupling constant $^{3}J_{HNH\alpha}$ and that calculated from the simulated ensembles.* Error bars are experimental uncertainty for NMR values as well as simulated standard deviations calculated for trajectories split into three sections. The coupling constants for the H^{α} protons of glycine are added to compare to experiment in which they are indistinguishable. (a) two parameterizations of the Karplus equation averaged over a single replica exchange ensemble using the TIP4P-Ew model. It is apparent that the dynamically uncorrected and harmonically corrected Karplus parameter sets work equally well on this disordered system. (b) average over the two independent replica exchange ensembles for different empirical force fields and compared to experimentally determined coupling constants. It is evident that an ensemble measurement gives far better agreement with the experimental $^{3}J_{HNH\alpha}$ values than that calculated from a single structure based on incorporating all of the ROESY restraints (shown in Figure 6).

Figure 3. *Normalized average vector time correlation function for Val24 C_α to H_α position for constant energy trajectories solvated with TIP4P-Ew and TIP3P.* The TIP3P model (blue) shows a dramatically faster decay for all vector time correlation functions relative to TIP4P-Ew (red), and we present this as an example. The inset presents example time correlation functions along with the triple exponential fits used in this study on a logarithmic y-axis to evaluate convergence. Presented are *Val24 C_α to H_α*, and *Ala21 $H_{\beta 1}$ to Asp23 H_N* as an example of a pair used for the relaxation experiment predictions and the ROESY peak predictions, respectively.

Figure 4. *Fingerprint region of ROESY spectrum in H_2O of $A\beta_{21-30}$.* (a) It is clear that the cross peak interpreted by Lazo et al. and Grant et al. as Hα Glu22 with HN Ala30 in their 500MHz experiments is clearly resolved as only Hα Lys28 to HN Ala30 in our 900MHz experiment. (b) HB3 Lys28 has a nearly overlapping chemical shift with HB2 Glu22, potentially leading to cross peak misassignment in previous studies at lower field[22].

Figure 5. *Representative structure from restraint energy minimized ensemble, simultaneously applying all observed ROE interactions*. *Peptide N-terminus is on the left side of all molecular drawings in this work.*

Figure 6. *Representative conformations of the ~30% populations with structure for the TIP4P-Ew/ff99SB.* (A) the most populated N-terminal hydrogen bond (dotted red) and (B) the hydrogen bonds and electrostatic interactions (dotted red) stabilizing the type I β-turn (cyan) centered at Val24 and Gly25.

Figure 7. *Representative conformation of the salt-bridge structure relevant for the protofibrils.* Asp23 to Lys28 salt-bridge (shown by red dotted line between aqua amino acids) found in 7% of the TIP4P-Ew ensemble, and Ala21 HB to Val24 HG (both in light blue) van der Waals contacts which give rise to the strongest observed ROE interaction.

TABLES

Table 1. ^{13}C NMR Spin Relaxation times T_1 and T_2 for non-glycine C_α positions from experiment and TIP4P-Ew, TIP3P and time scaled TIP4P-Ew, in milliseconds. Glu22 and Lys28 resonances overlapped such that T_1 and T_2 could not be independently measured. The relaxation times calculated from the overlapped peaks are indicated with an asterisk.

		A21	E22	D23	V24	S26	N27	K28	A30
T1	**Experiment**	415	298*	244	291	285	274	298*	475
at	**TIP4P-Ew**	492	292	268	272	274	273	287	530
500MHz	**Scaled**	457	276	253	260	262	261	275	485
	TIP3P	853	469	398	389	386	396	413	907
T2	**Experiment**	403	265*	269	230	235	241	265*	372
at	**TIP4P-Ew**	445	262	248	236	245	239	242	475
600MHz	**Scaled**	398	238	225	215	224	218	220	425
	TIP3P	860	474	403	386	386	393	402	858

Table 2. Proton cross-peak predictions for TIP3P and TIP4P-Ew for the 900MHz spectra in H_2O. Experimental intensities (Iexp) are normalized to the intensity of the weakest assigned peak. Simulation intensities (Isim) are normalized to experimental intensity as described in Methods. Experimental intensities are labeled as a dash if the peak is absent or "<1.0" if some evidence of a peak is present but is too weak to be assigned. Simulated intensities are marked with a # if the H_2O prediction is found in the ^2H_2O experiment.

TIP3P

Isim	Iexp	Proton 1		Proton 2	
5.4	<1.0	HA	VAL24	HB3	ASN27
4.4	#1.8	HB3	ASP23	HB2	SER26
4.0	-	HA	ASP23	H	GLY25
3.0	2.6	HG	VAL24	H	SER26
2.8	15.7	HB	ALA21	HG	VAL24
2.7	<1.0	HG3	GLU22	H	VAL24
2.7	-	HB3	ASP23	H	SER26
2.7	-	HA	GLU22	HA	ASN27
2.6	2.9	HB	ALA21	H	ASP23
2.6	-	HA	VAL24	H	ASN27
2.6	1.3	HB3	ASP23	H	GLY25
2.4	4.9	HG3	GLU22	HG	VAL24
2.3	#1.4	HA	VAL24	HB2	ASN27
2.0	2.6	HA	VAL24	H	SER26
2.0	1.2	HA	GLY25	H	ASN27
1.6	-	HA	ASN27	H	GLY29
1.4	#3.8	HB3	GLU22	HG	VAL24
1.4	7.2	HG2	GLU22	HG	VAL24
1.4	2.8	HG	VAL24	HB3	ASN27
1.4	-	1HD2	ASN27	H	GLY29
1.4	-	HB3	GLU22	H	VAL24
1.3	-	HA	ASP23	HA	LYS28
1.3	-	HB3	ASP23	HE2	LYS28
1.2	-	HG	VAL24	H	ASN27
1.2	2.6	HG	VAL24	HB2	ASN27
1.2	-	H	VAL24	H	SER26
1.2	#2.4	HB2	GLU22	HG	VAL24
1.2	-	1HD2	ASN27	HA	GLY29
1.2	-	H	ASP23	HB2	SER26
1.2	-	HG2	GLU22	HA	ASN27
1.1	-	HG3	LYS28	H	ALA30
1.1	-	HB3	ASN27	H	GLY29
1.1	-	HB	ALA21	HA	ASN27
1.0	-	HA	GLU22	H	LYS28
1.0	-	H	ASP23	H	SER26
1.0	-	H	GLY25	H	ASN27
1.0	-	HB	ALA21	HB2	SER26
1.0	-	HA	ASP23	H	SER26
1.0	-	HG	VAL24	HA	GLY29
False Negatives:					
0.9	1.1	HA	SER26	H	LYS28
0.6	3.8	HA	GLY25	HD2	LYS28
0.6	3.8	HB3	ASN27	HB	ALA30
0.5	1.7	HA	LYS28	H	ALA30
0.3	2.5	HB3	LYS28	H	ALA30
0.3	1.1	HB2	ASN27	H	GLY29
0.0	3.3	HB2	ASN27	HB	ALA30

TIP4P-Ew

Isim	Iexp	Proton 1		Proton 2	
4.1	15.7	HB	ALA21	HG	VAL24
2.8	2.6	HG	VAL24	H	SER26
2.6	2.9	HB	ALA21	H	ASP23
1.9	4.9	HG3	GLU22	HG	VAL24
1.9	1.3	HB3	ASP23	H	GLY25
1.7	<1.0	HG3	GLU22	H	VAL24
1.6	-	2HD2	ASN27	H	GLY29
1.3	-	HB3	GLU22	H	VAL24
1.3	#2.4	HB2	GLU22	HG	VAL24
1.3	-	HA	GLU22	HA	ASN27
1.3	1.2	HA	GLY25	H	ASN27
1.3	#1.4	HA	VAL24	HB2	ASN27
1.2	<1.0	HA	VAL24	HB3	ASN27
1.2	#1.8	HB3	ASP23	HB2	SER26
1.2	2.6	HA	VAL24	H	SER26
1.1	-	HG	VAL24	H	ASN27
1.1	-	2HD2	ASN27	HA	GLY29
1.1	#3.8	HB3	GLU22	HG	VAL24
1.1	7.2	HG2	GLU22	HG	VAL24
1.0	-	HB	VAL24	H	SER26
1.0	-	HB3	ASP23	H	SER26
False Negatives:					
0.9	1.1	HB2	ASN27	H	GLY29
0.7	2.8	HG	VAL24	HB3	ASN27
0.6	2.6	HG	VAL24	HB2	ASN27
0.5	3.3	HB2	ASN27	HB	ALA30
0.4	1.7	HA	LYS28	H	ALA30
0.4	3.8	HA	GLY25	HD2	LYS28
0.2	2.5	HB3	LYS28	H	ALA30
0.0	1.1	HA	SER26	H	LYS28
0.0	3.8	HB3	ASN27	HB	ALA30

Table 3. Proton cross-peak predictions for TIP3P and TIP4P-Ew for the 800MHz spectra in $^{2}H_2O$. See Table 2 for additional details.

TIP3P						TIP4P-Ew					
						Isim	Iexp	Proton 1		Proton 2	
11.7	<1.0	HA	VAL24	HB3	ASN27	8.0	7.4	HB	ALA21	HG	VAL24
10.0	1.8	HB3	ASP23	HB2	SER26	3.9	5.1	HG3	GLU22	HG	VAL24
6.1	-	HA	GLU22	HA	ASN27	3.1	-	HA	GLU22	HA	ASN27
5.8	7.4	HB	ALA21	HG	VAL24	3.0	1.4	HA	VAL24	HB2	ASN27
5.0	5.1	HG3	GLU22	HG	VAL24	2.8	1.8	HB3	ASP23	HB2	SER26
5.0	1.4	HA	VAL24	HB2	ASN27	2.7	<1.0	HA	VAL24	HB3	ASN27
3.0	3.8	HB3	GLU22	HG	VAL24	2.7	2.4	HB2	GLU22	HG	VAL24
3.0	1.8	HG	VAL24	HB3	ASN27	2.3	3.8	HB3	GLU22	HG	VAL24
3.0	4.3	HG2	GLU22	HG	VAL24	2.2	4.3	HG2	GLU22	HG	VAL24
2.9	-	HA	ASP23	HA	LYS28	2.2	0.8	HA	GLU22	HG	VAL24
2.7	-	HB3	ASP23	HE2	LYS28	1.8	-	HB	VAL24	HB2	ASN27
2.5	-	HG2	GLU22	HA	ASN27	1.6	1.3	HG	VAL24	HB2	SER26
2.5	1.6	HG	VAL24	HB2	ASN27	1.5	1.8	HG	VAL24	HB3	ASN27
2.5	2.4	HB2	GLU22	HG	VAL24	1.5	3.1	HG	VAL24	HE2	LYS28
2.4	-	HB	ALA21	HA	ASN27	1.5	-	HB3	ASP23	HA	LYS28
2.3	-	HA	VAL24	HA	ASN27	1.4	-	HG	VAL24	HA	SER26
2.2	-	HB	ALA21	HB2	SER26	1.4	1.6	HG	VAL24	HB2	ASN27
2.1	-	HG	VAL24	HA	GLY29	1.4	-	HA	VAL24	HB2	LYS28
2.0	-	HA	GLY25	HA	GLY29	1.4	-	HG2	GLU22	HA	ASN27
2.0	3.1	HG	VAL24	HE2	LYS28	1.3	-	HB	ALA21	HB2	SER26
1.9	-	HB3	ASP23	HG3	LYS28	1.3	-	HA	SER26	HE2	LYS28
1.8	-	HA	GLU22	HA	GLY29	1.3	-	HB	ALA21	HB3	ASP23
1.8	1.3	HG	VAL24	HB2	SER26	1.3	-	HB	ALA21	HA	ASP23
1.8	-	HG3	GLU22	HB2	SER26	1.2	-	HG	VAL24	HA	ASN27
1.8	-	HG3	LYS28	HB	ALA30	1.2	-	HA	GLY25	HE2	LYS28
1.6	-	HG2	GLU22	HB2	ASN27	1.1	0.9	HG	VAL24	HA	LYS28
1.6	-	HG	VAL24	HD2	LYS28	1.1	-	HB2	SER26	HE2	LYS28
1.6	0.8	HA	GLU22	HG	VAL24	1.0	-	HA	ASP23	HB2	SER26
1.6	-	HG3	GLU22	HA	ASN27	1.0	-	HB	ALA21	HA	SER26
1.5	-	HG	VAL24	HB3	SER26	1.0	2.5	HB2	ASN27	HB	ALA30
1.5	-	HB	ALA21	HB	ALA30	1.0	-	HG	VAL24	HB3	SER26
1.5	-	HB2	SER26	HE2	LYS28						
1.5	-	HA	GLY25	HE2	LYS28	False Negatives:					
1.4	-	HB2	GLU22	HA	GLY29	0.9	1.8	HA	GLY25	HD2	LYS28
1.3	-	HA	ASP23	HB2	SER26	0.4	1.0	HB3	SER26	HG3	LYS28
1.3	1.8	HA	GLY25	HD2	LYS28	0.1	2.2	HB3	ASP23	HB3	SER26
1.3	-	HB3	ASP23	HB2	LYS28	-0.1	0.8	HB2	ASP23	HB3	SER26
1.3	-	HB	VAL24	HB3	ASN27	-0.1	3.9	HB3	ASN27	HB	ALA30
1.2	-	HB	ALA21	HB2	ASN27	-0.3	1.7	HB2	ASP23	HB2	SER26
1.2	-	HA	SER26	HE2	LYS28						
1.2	-	HG	VAL24	HA	ASN27						
1.2	-	HA	GLU22	HA	LYS28						
1.2	3.9	HB3	ASN27	HB	ALA30						
1.2	-	HB	ALA21	HB3	ASP23						
1.2	2.2	HB3	ASP23	HB3	SER26						
1.2	-	HB3	ASP23	HD2	LYS28						
1.2	-	HB2	SER26	HG3	LYS28						
1.1	-	HB3	ASP23	HA	GLY25						
1.1	-	HE2	LYS28	HB	ALA30						
1.1	-	HB	ALA21	HB2	LYS28						
1.1	-	HB3	GLU22	HA	ASN27						
1.1	-	HB3	ASP23	HG2	LYS28						
1.1	-	HG	VAL24	HA	SER26						
1.0	-	HA	VAL24	HE2	LYS28						
1.0	-	HB	ALA21	HA	ASP23						

```
 1.0      -    | HG3  GLU22   | HB2  ASN27
 1.0      -    | HB   ALA21   | HA   ALA30
 1.0      -    | HB3  GLU22   | HB2  ASN27
 1.0      -    | HB   ALA21   | HA   VAL24
 1.0      -    | HG2  GLU22   | HA   GLY29
False Negatives:
 0.9     1.0   | HG   VAL24   | HA   LYS28
 0.3     1.0   | HB3  SER26   | HG3  LYS28
 0.1     2.5   | HB2  ASN27   | HB   ALA30
 0.0     0.8   | HB2  ASP23   | HB3  SER26
-0.7     1.7   | HB2  ASP23   | HB2  SER26
```

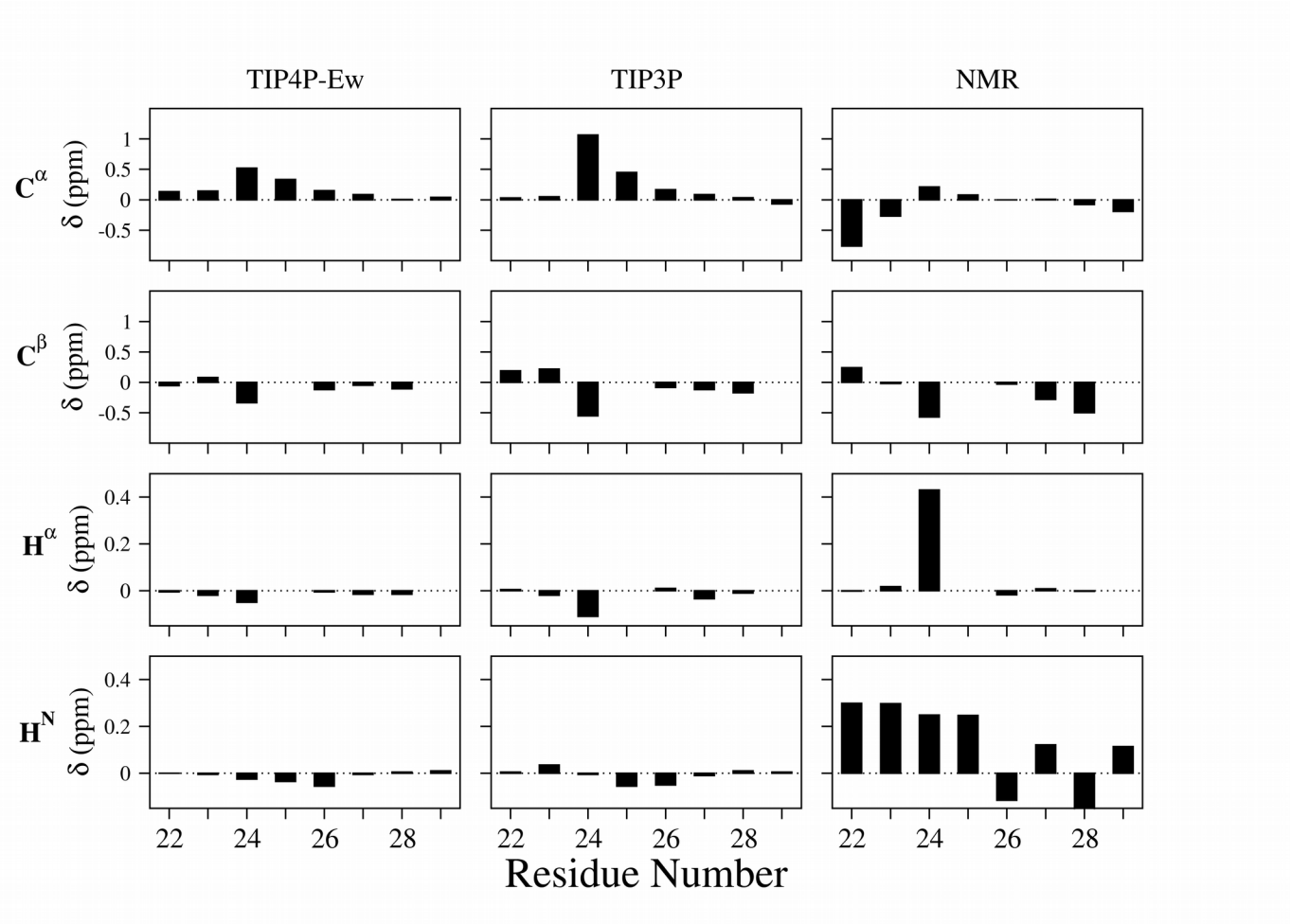

Figure 1. Fawzi et al.

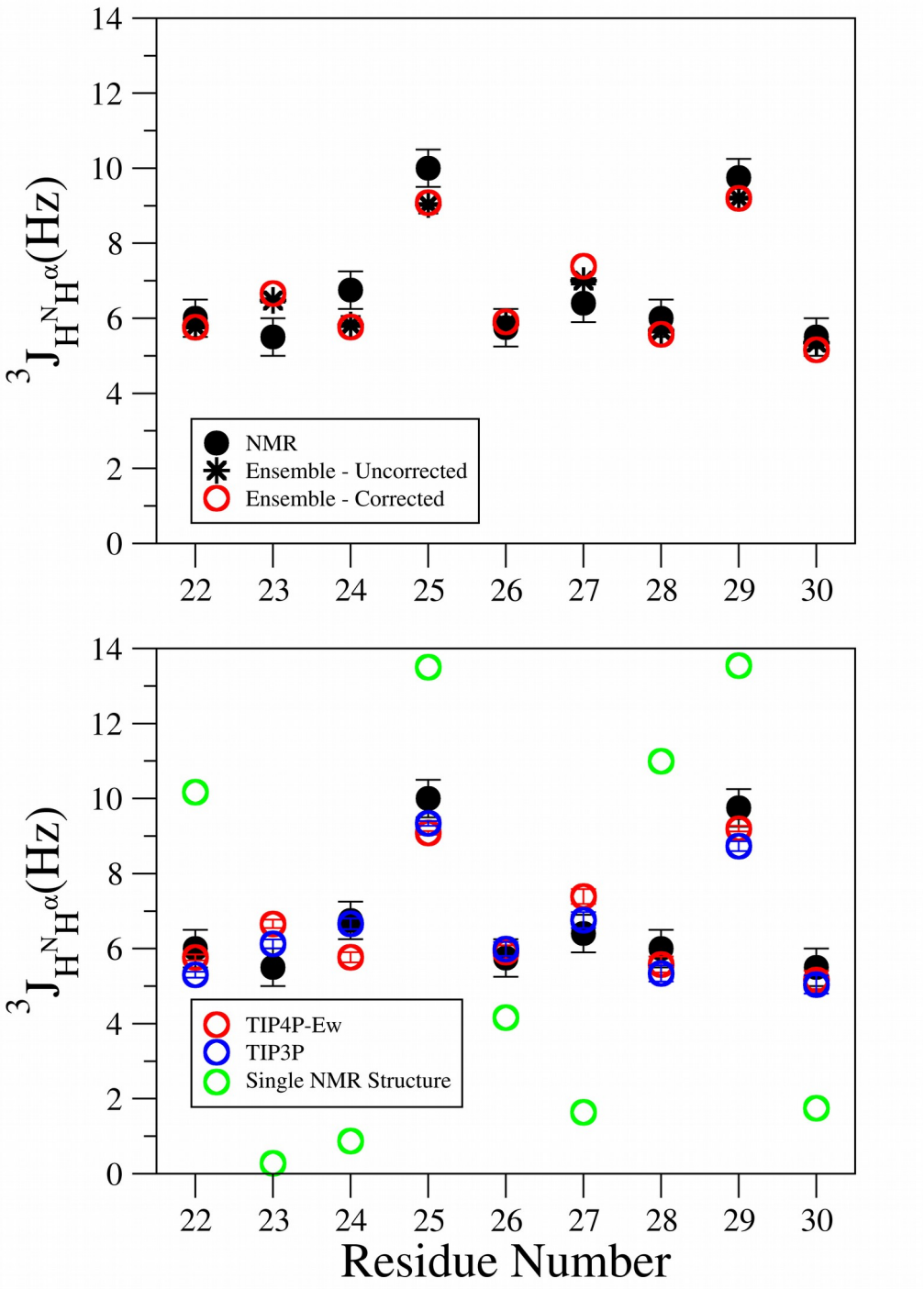
14
12
10
8
6
4
2
0
$^3J_{H^NH^\alpha}$(Hz)
NMR
Ensemble - Uncorrected
Ensemble - Corrected
22
23
24
25
26
27
28
29
30
TIP4P-Ew
TIP3P
Single NMR Structure
Residue Number

Figure 2. Fawzi et al.

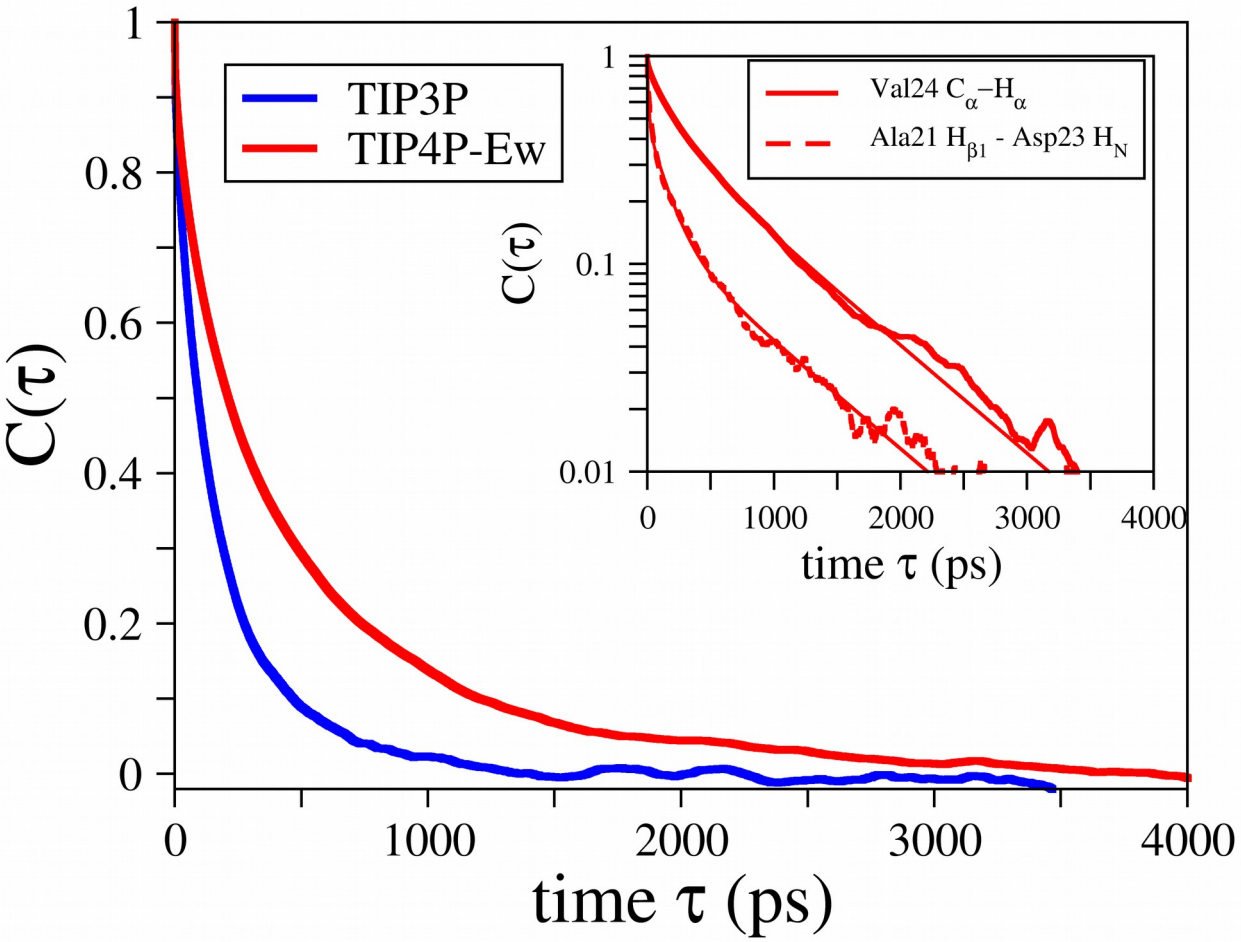

Figure 3. Fawzi et al.

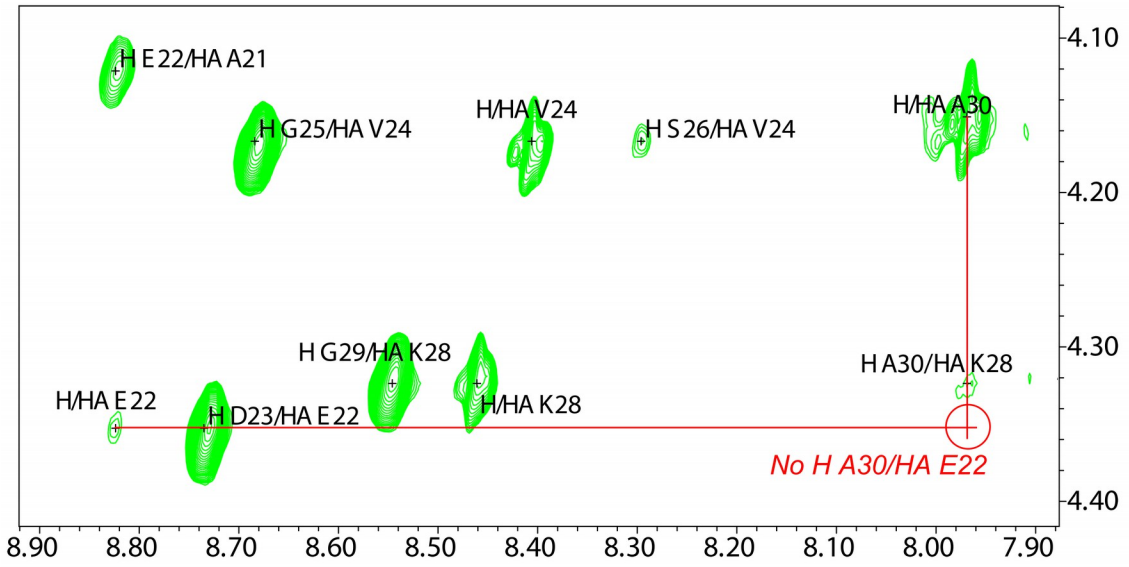
H E22/HA A21
H G25/HA V24
H/HA V24
H S26/HA V24
H/HA A30
H G29/HA K28
H A30/HA K28
H/HA E22
H D23/HA E22
H/HA K28
No H A30/HA E22
4.10
4.20
4.30
4.40
8.90
8.80
8.70
8.60
8.50
8.40
8.30
8.20
8.10
8.00
7.90

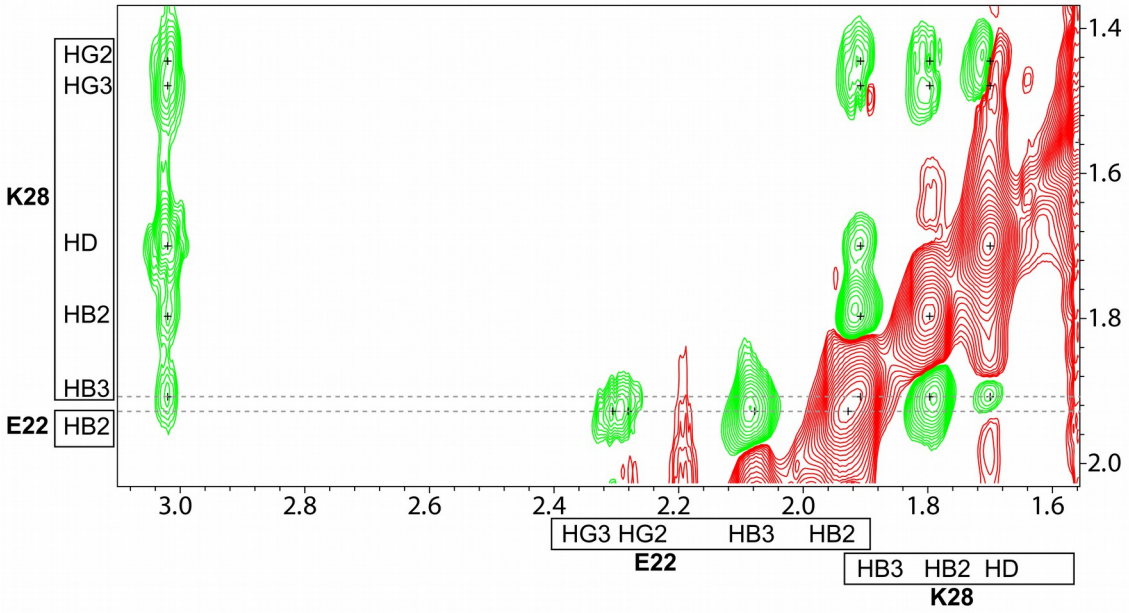
HG2
HG3
K28
HD
HB2
HB3
E22
HB2
1.4
1.6
1.8
2.0
3.0
2.8
2.6
2.4
2.2
2.0
1.8
1.6
HG3 HG2 HB3 HB2
E22
HB3 HB2 HD
K28

Figure 4. Fawzi et al.

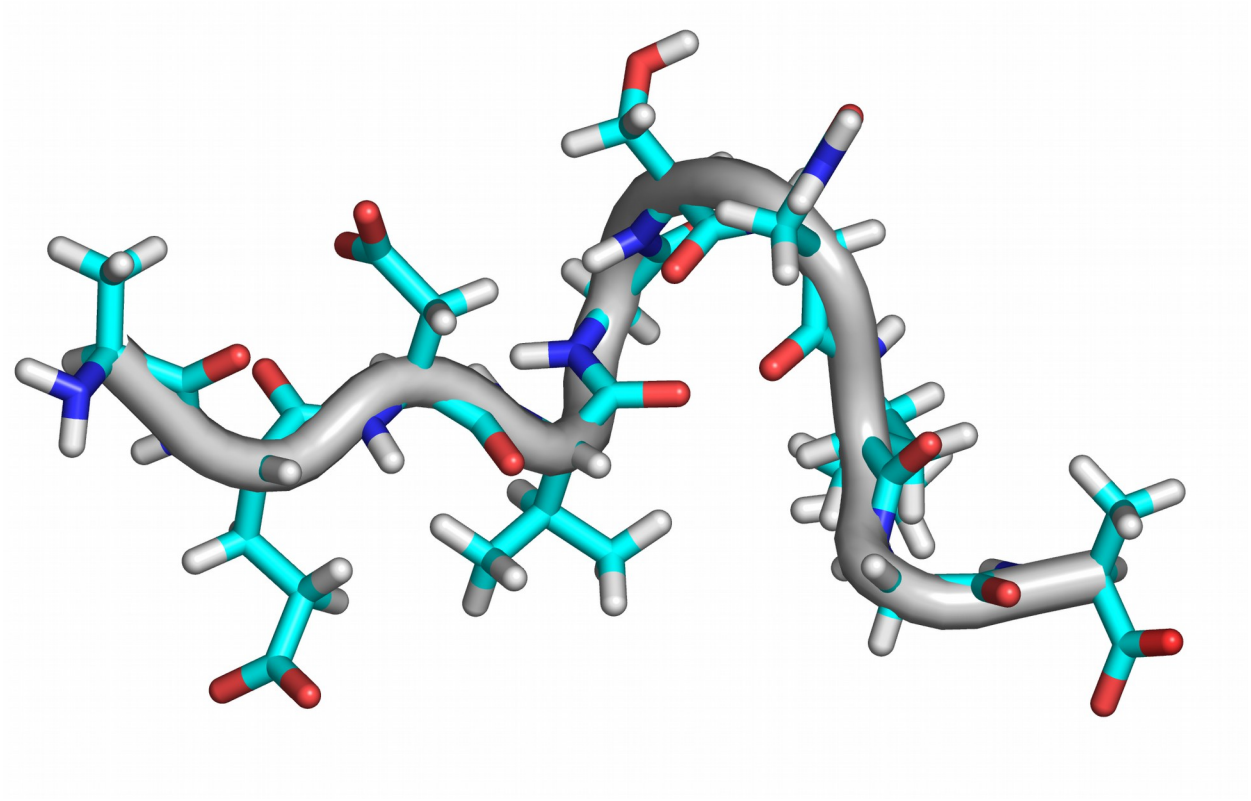

Figure 5. Fawzi et al.

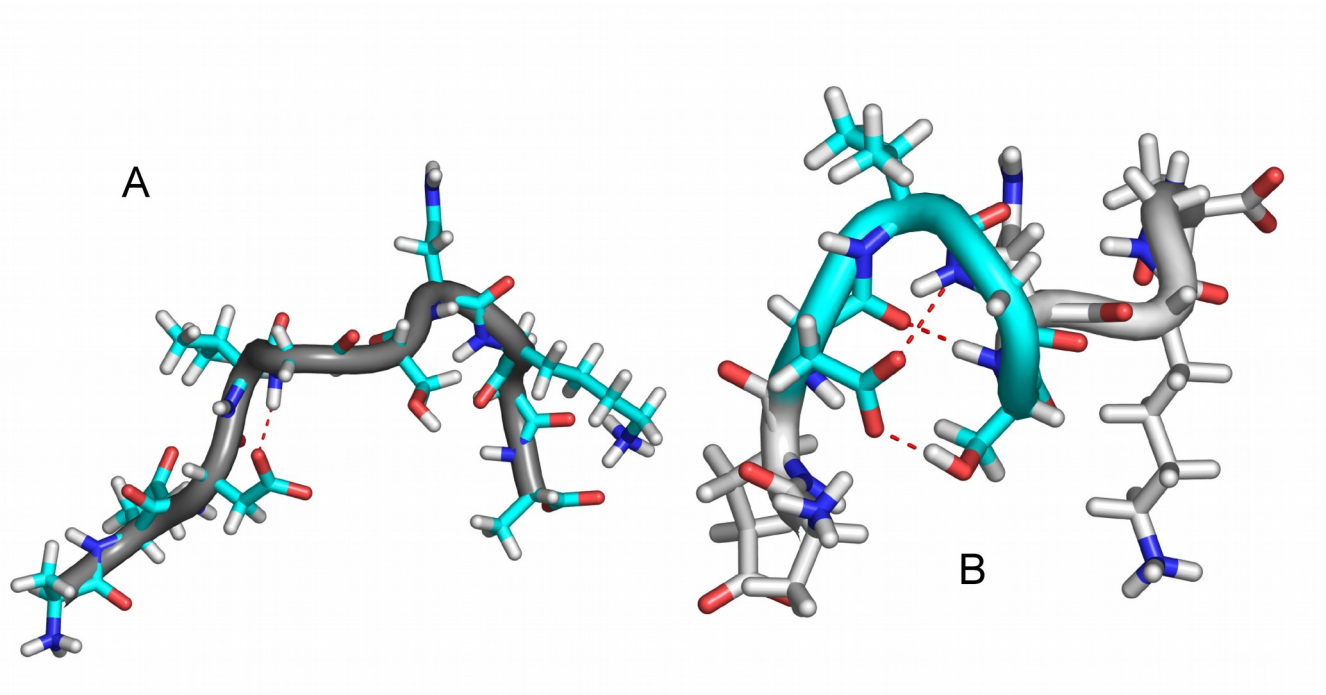

Figure 6. Fawzi et al.

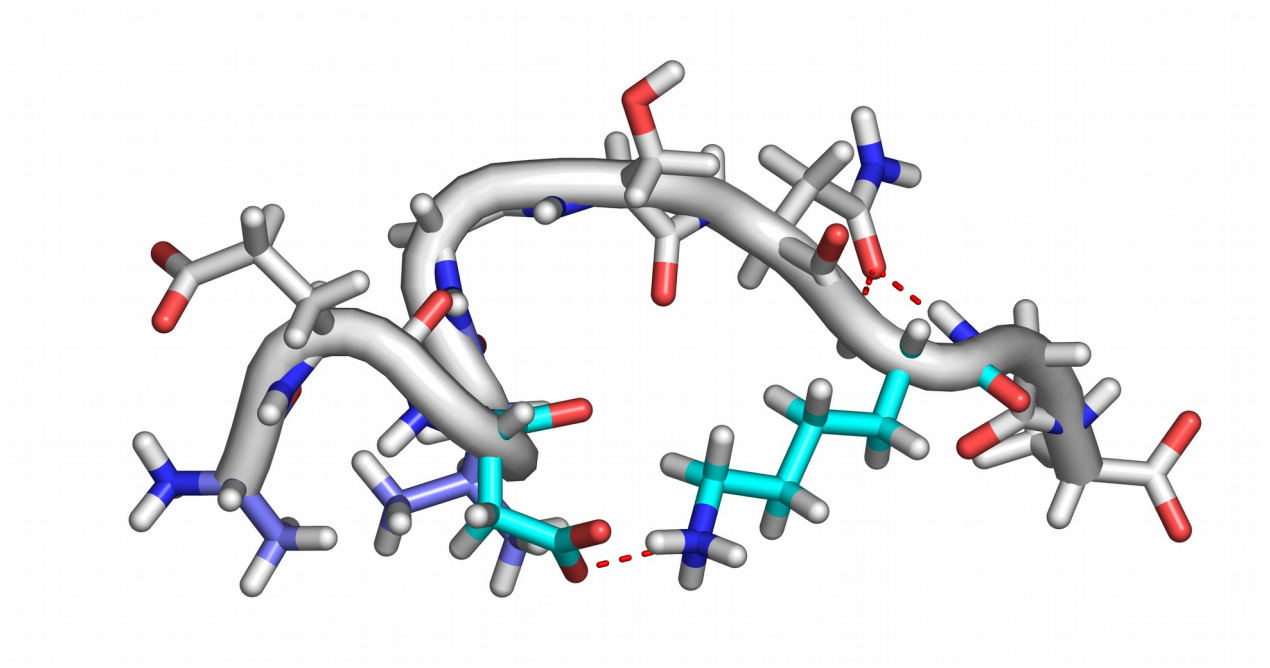

Figure 7. Fawzi et al.

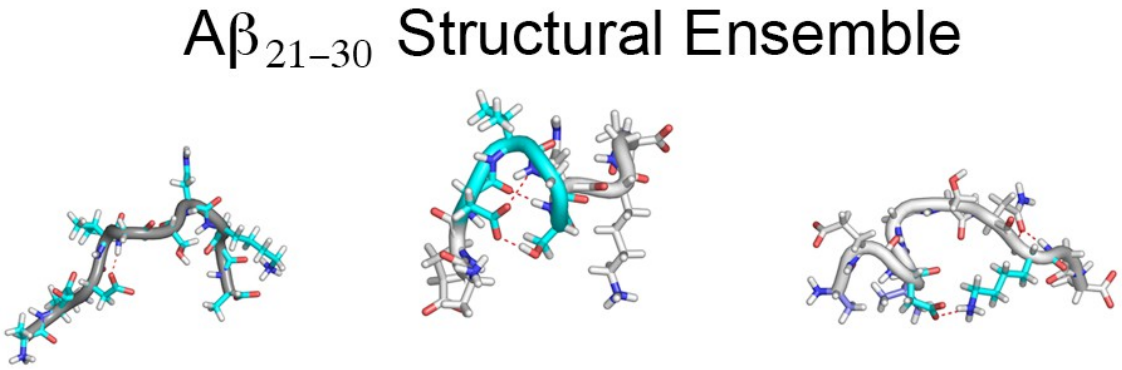

TOC Graphic. Fawzi et al.